Polyhedral finite elements for nonlinear solid mechanics using tetrahedral subdivisions and dual-cell aggregation

Joseph E. Bishop[a], N. Sukumar[b]

[a]*Engineering Sciences Center, Sandia National Laboratories, Albuquerque, NM 87185, U.S.A.*
[b]*Department of Civil & Environmental Engineering, University of California, Davis, CA 95616, U.S.A.*

Abstract

General polyhedral discretizations offer several advantages over classical approaches consisting of standard tetrahedra and hexahedra. These include increased flexibility and robustness in the meshing of geometrically complex domains and higher-quality solutions for both finite element and finite volume schemes. Currently, the use of general polyhedra is hampered by the lack of general-purpose polyhedral meshing algorithms and software. One approach for generating polyhedral meshes is the use of tetrahedral subdivisions and dual-cell aggregation. In this approach, each tetrahedron of an existing tetrahedral mesh is subdivided using one of several subdivision schemes. Polyhedral-dual cells may then be formed and formulated as finite elements with shape functions obtained through the use of generalized barycentric coordinates. We explore the use of dual-cell discretizations for applications in nonlinear solid mechanics using a displacement-based finite element formulation. Verification examples are presented that yield optimal rates of convergence. Accuracy of the methodology is demonstrated via several nonlinear examples that include large deformation and plasticity.

Keywords: finite element, polyhedra, nonlinear, large deformation, dual cell, tetrahedra

1. Introduction

Several finite element formulations now exist for general polyhedral elements, ones with arbitrary number of vertices and faces, generally nonconvex, and with possibly nonplanar faces (Rashid and Selimotic, 2006; Bishop, 2014; Beirão da Veiga et al., 2013; Gain et al., 2014; Chi et al., 2017; Talebi et al., 2016; Liu et al., 2017; Sohn et al., 2012, 2013; Kim and Sohn, 2015). However, despite recent research in the development of polyhedral finite element formulations, the development of general purpose polyhedral meshing tools is lacking. Examples include hybrid meshing (hex dominant) (Oaks and Paoletti, 2000; Sokolov et al., 2016; Gao et al., 2017), cut-cell approaches (Sohn et al., 2012, 2013; Kim and Sohn, 2015), and Voronoi techniques (Abdelkader et al., 2019). Boundary-conforming Voronoi meshes can be challenging to generate on complex domains. Furthermore, both Voronoi and cut-cell meshes can cause difficulties in numerical simulations due to the presence of small edges and faces. Another approach to meshing is to start with a tetrahedral mesh, possible of low quality, and then aggregate into polyhedra. This has been explored in the context of meshfree methods by Millán et al. (2015); Koester and Chen (2019) and discontinuous Galerkin methods by Bassi et al. (2012). The construction of polyhedral-dual meshes from tetrahedral meshes has been explored by a number of authors (Balafas, 2014; Garimella et al., 2014; Lee, 2015). Rimoli and Ortiz (2011) have used polyhedral-dual cells of tetrahedra in the mesoscale modeling of polycrystalline materials.

Here, we explore the use of polyhedral-dual cells of a pre-existing tetrahedral mesh (the primal mesh) to form a polyhedral mesh suitable for finite element analysis. In this approach, each tetrahedron is first subdivided using one of several possible subdivision schemes. The resulting pieces are then either used directly (as a polyhedron) or aggregated into larger polyhedra. The shape quality of the polyhedral-dual elements is inherited from the initial tetrahedral elements. The resulting polyhedral elements, although generally nonconvex, have planar faces thus allowing for the use of several types of shape functions. We

use harmonic and maximum-entropy (max-ent) shape functions, both of which are a type of optimization-based shape function. The harmonic shape functions minimize a functional of the norm of the gradient whereas max-ent shape functions minimize a certain relative entropy functional. Our primary application is nonlinear solid mechanics, so we seek to minimize the number of quadrature points per element without inducing zero or near-zero energy modes. A key research question, beyond the scope of this work, is how does the efficiency and robustness of this polyhedral discretization compare to using the tetrahedral mesh directly for nonlinear solid mechanics (Danielson, 2014; Ostien et al., 2016).

This paper is structured as follows. Section 2 reviews the governing equations for solid mechanics and the weak formulation. Section 3 discusses the concepts of tetrahedral subdivision and dual-cell aggregation. The polyhedral finite element formulation is presented in Section 4. Verification examples are presented in Section 5. These include the engineering patch test, convergence examples for linear elasticity, and the Cook's membrane problem in the nearly incompressible regime of material behavior. Several boundary-value problems, both static and dynamic, are presented in Section 6. Finally, we conclude with our main findings in Section 7.

2. Governing equations

Consider the motion of a body $\mathcal{B}$ with interior domain Ω and boundary Γ subjected to applied surface tractions $\boldsymbol{t}$ per unit area. We assume that there are no externally applied body forces. A Lagrangian description of the motion of $\mathcal{B}$ is used. The initial configuration of the body is denoted by $\mathcal{B}_0$ with interior Ω_0 and boundary Γ_0. In the initial configuration, the position vector of a material point is denoted by $\boldsymbol{X}$. In the deformed configuration, the position of a material point is denoted by $\boldsymbol{x}$. The displacement vector $\boldsymbol{u}$ is then given by $\boldsymbol{u} := \boldsymbol{x} - \boldsymbol{X}$.

2.1. Conservation of mass

The deformation gradient $\boldsymbol{F}$ is defined as the material derivative of $\boldsymbol{x}$ with respect to $\boldsymbol{X}$ so that $\boldsymbol{F} := \partial\boldsymbol{x}/\partial\boldsymbol{X} = \partial\boldsymbol{u}/\partial\boldsymbol{X} + \boldsymbol{I}$, where $\boldsymbol{I}$ is the identity tensor. The initial and current mass densities are denoted by ρ_0 and ρ, respectively. The Jacobian J of the deformation gradient $\boldsymbol{F}$ is given by its determinant, $J = \det \boldsymbol{F}$. The conservation of mass can then be expressed as (Belytschko et al., 2014; Bonet and Wood, 2008)

$$\rho_0 = \rho\, J\,. \tag{1}$$

2.2. Conservation of momentum

The shape functions of the polyhedral elements described in Section 4 will be constructed directly on the initial configuration of the element. Therefore, a *total*-Lagrangian formulation of the governing equations is appropriate. In the absence of body forces, the conservation of linear momentum is given by (Belytschko et al., 2014; Bonet and Wood, 2008)

$$\frac{\partial \boldsymbol{P}}{\partial \boldsymbol{X}} : \boldsymbol{I} = \rho_0\, \ddot{\boldsymbol{u}} \tag{2}$$

with boundary conditions

$$\boldsymbol{u} = \overline{\boldsymbol{u}} \quad \text{on} \quad \Gamma_0^u \quad \text{and} \quad \boldsymbol{P}\cdot\boldsymbol{N} = \boldsymbol{t}_0 \quad \text{on} \quad \Gamma_0^t\,,$$

where $\boldsymbol{P}$ is the first Piola-Kirchhoff stress tensor, $\ddot{\boldsymbol{u}}$ is the acceleration vector, $\boldsymbol{N}$ is the outward unit normal on Γ_0, $\boldsymbol{t}_0$ is the surface traction vector per unit initial area, and $\overline{\Gamma_0^u \cup \Gamma_0^t} = \Gamma_0$ and $\Gamma_0^u \cap \Gamma_0^t = \emptyset$.

The first Piola-Kirchhoff stress tensor $\boldsymbol{P}$ is related to the Cauchy stress tensor $\boldsymbol{\sigma}$ (true stress) by the expression $\boldsymbol{P} = J\,\boldsymbol{\sigma}\,\boldsymbol{F}^{-T}$, where the notation $(\,\cdot\,)^{-T}$ represents the composition of the transpose and inverse operators. Conservation of angular momentum follows from the symmetry of $\boldsymbol{\sigma}$.

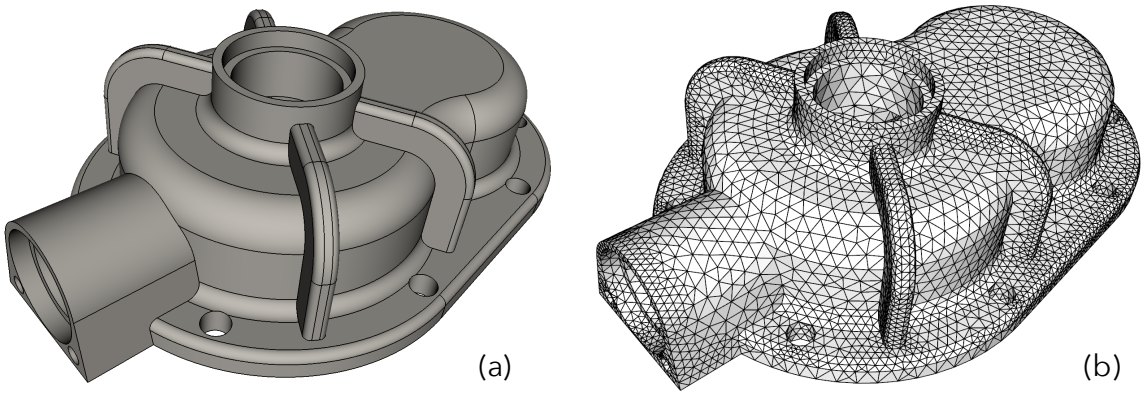

Figure 1: (a) Geometry definition of a machine part and (b) tetrahedral mesh (11, 851 vertices, 46, 789 tetrahedra).

2.3. Weak form

The weak form of (2) is given by the following variational problem (Belytschko et al., 2014; Bonet and Wood, 2008): find the trial functions $\boldsymbol{u} \in \boldsymbol{H}^1(\Omega_0)$, where $\boldsymbol{H}^1(\Omega_0) := [H^1(\Omega_0)]^3$, with $\boldsymbol{u} = \overline{\boldsymbol{u}}$ on Γ_0^u such that

$$\int_{\Gamma_0^t} \boldsymbol{t}_0 \cdot \boldsymbol{v}\, dS - \int_{\Omega_0} \boldsymbol{P} : (\partial \boldsymbol{v}/\partial \boldsymbol{X})\, d\boldsymbol{X} = \int_{\Omega_0} \rho_0\, \ddot{\boldsymbol{u}} \cdot \boldsymbol{v}\, d\boldsymbol{X} \tag{3}$$

for all test functions $\boldsymbol{v} \in \boldsymbol{H}_0^1(\Omega_0)$. Here, $H^1(\Omega_0)$ is the Sobolev function space of degree one containing functions that possess square-integrable weak derivatives, and the Sobolev space $\boldsymbol{H}_0^1(\Omega_0) := \{\boldsymbol{v} \in \boldsymbol{H}^1(\Omega_0) : \boldsymbol{v} = 0 \text{ on } \Gamma_0^u\}$.

The Galerkin procedure for obtaining an approximate solution to (3) uses a finite dimensional approximation to $\boldsymbol{H}^1(\Omega_0)$, denoted by $\boldsymbol{V}^h$, with $\boldsymbol{V}^h \subset \boldsymbol{H}^1(\Omega_0)$ and $\boldsymbol{V}_0^h = \{\boldsymbol{v}^h \in \boldsymbol{V}^h \,|\, \boldsymbol{v}^h = 0 \text{ on } \Gamma_0^u\}$. Let $\{\phi_I, I = 1, \ldots, N\}$ be a basis for V^h so that any $\boldsymbol{u}^h \in \boldsymbol{V}^h$ may be written as $\boldsymbol{u}^h(\boldsymbol{X}) = \sum_{I=1}^N \phi_I(\boldsymbol{X})\, \boldsymbol{u}_I$. A finite element approximation entails choosing basis functions $\phi_I(\boldsymbol{X})$ with local support defined by a mesh. Let Ω_e represent the domain of a finite element in the initial configuration with boundary Γ_e and vertex (nodal) coordinates $\boldsymbol{X}_a$, $a = 1, \ldots, N_\mathrm{v}$, where N_v is the number of vertices of the polyhedral element. The basis functions may be decomposed into element shape functions denoted as $\psi_a(\boldsymbol{X})$.

A conventional finite element mesh consists of hexahedra or tetrahedra. In this work, we instead consider a mesh comprised of more general polyhedra defined through a process of tetrahedral subdivision and aggregation as described in Section 3. The construction of the element shape functions and their derivatives is described in Section 4 along with a consistent integration scheme for approximating the integrals in (3).

3. Tetrahedral subdivision and aggregation

Our method of polyhedral meshing relies on an initial tetrahedral mesh of the given domain. An example tetrahedral mesh of a machine part is shown in Fig. 1. Each tetrahedral element is then subdivided using one of three types of tetrahedral subdivision: (1) barycentric (also called median subdivision), (2) full truncation (also called rectification), and (3) partial truncation. These three subdivision methods are illustrated in Fig. 2. The resulting mesh decomposition may then be partitioned into dual cells and formulated as polyhedral finite elements. Barycentric subdivision is discussed in Section 3.1. Truncation subdivision is discussed in Section 3.2.

3.1. Barycentric subdivision

Polyhedral meshing through barycentric subdivision (medial mesh) has been studied by Balafas (2014) and Garimella et al. (2014). The barycentric subdivision process in two dimensions is illustrated in Fig. 3. Each triangle is first subdivided into three quadrilaterals through the introduction of an additional vertex

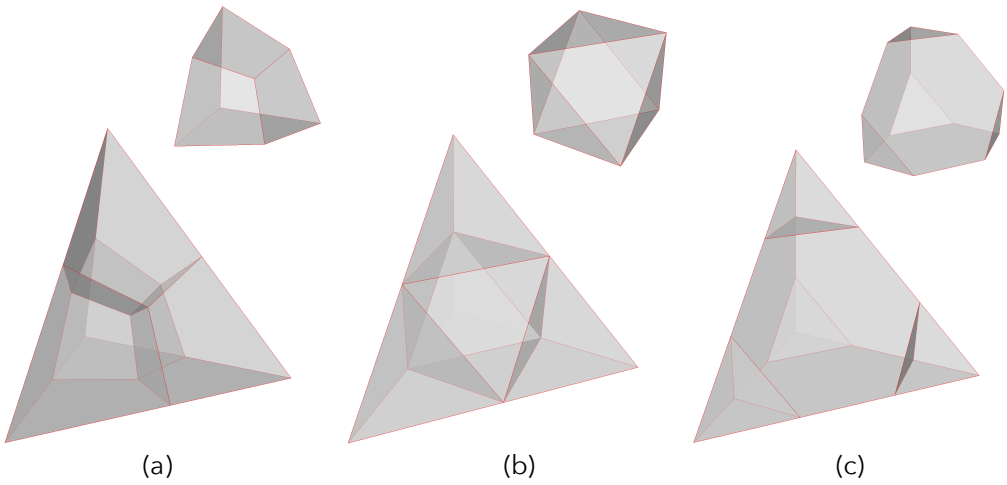

Figure 2: Three types of tetrahedral subdivisions: (a) barycentric subdivision, (b) full truncation (rectification), and (c) partial truncation. Barycentric subdivision creates four sub-hexahedra (inset). Full truncation creates four sub-tetrahedra and a 6-vertex octahedron (inset). Partial truncation creates four sub-tetrahedra and a 12-vertex octahedron (inset).

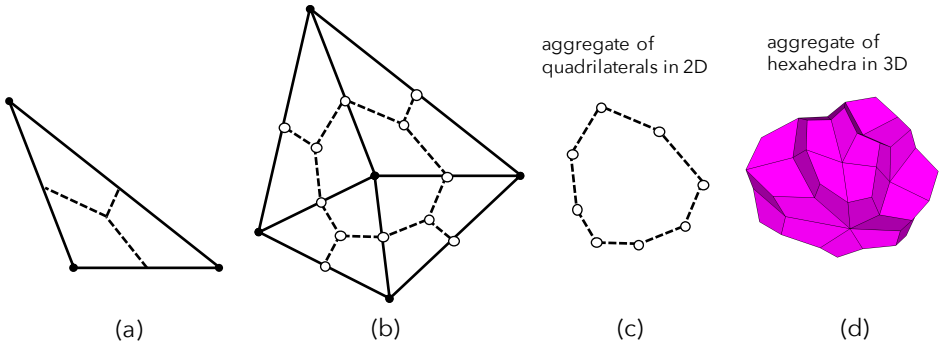

Figure 3: Method of constructing type-1 polyhedral-dual elements using barycentric subdivision in two dimensions. (a) Original triangle and a barycentric subdivision, (b) triangle patch and barycentric subdivision, (c) resulting polygonal-dual cell, and (d) example three-dimensional polyhedral-dual cell consisting of sub-hexahedra.

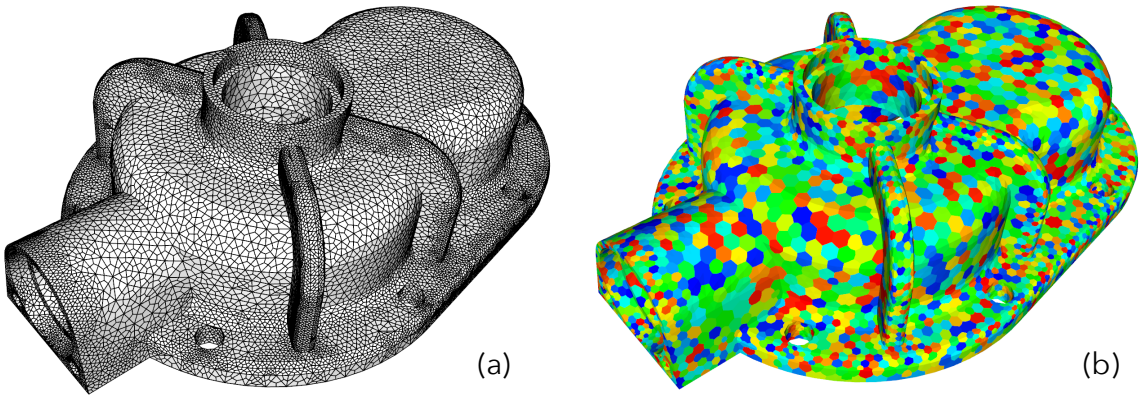

Figure 4: Type-1 polyhedral-dual mesh of the example machine part shown in Fig. 1. (a) Mesh (222, 548 vertices, 11, 851 polyhedra) and (b) random coloring of polyhedral elements.

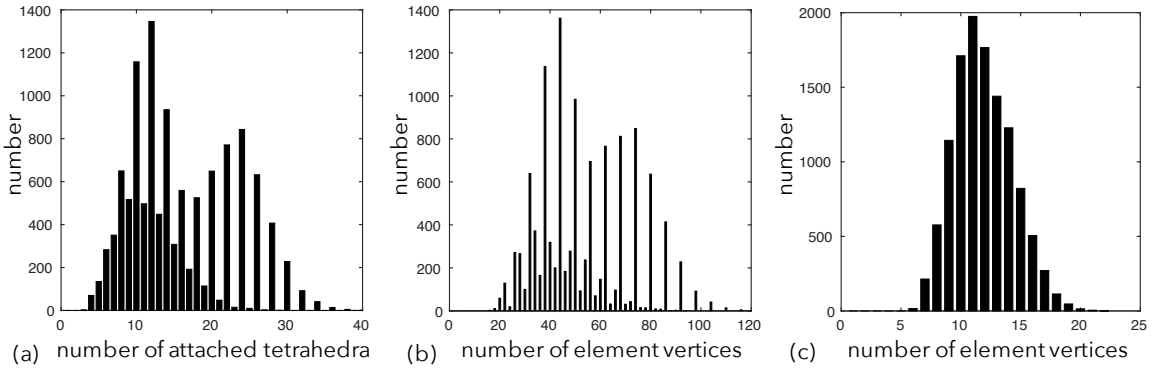

Figure 5: Histograms of the various meshes (tetrahedral and polyhedral dual) of the example machine part shown in Fig. 1. (a) Number of attached tetrahedra to a node in the original tetrahedral mesh, (b) number of element vertices for the type-1 polyhedral-dual mesh shown in Fig. 4, and (c) number of element vertices for the type-2 and type-3 polyhedral-dual meshes (polytet elements only).

at the centroid (barycenter) and additional vertices at the midpoint of each edge as shown in Fig. 3a and Fig. 3b. A polygonal-dual cell may then be formed by aggregating the quadrilaterals attached to each original triangle vertex as shown in Fig. 3c. In three dimensions, each tetrahedron is first subdivided into four hexahedra by using edge midpoints, face centroids, and the element centroid as shown in Fig. 2a. A polyhedral-dual cell is then formed by aggregating the hexahedra attached to each original vertex. A three-dimensional dual cell is shown in Fig. 3d. Note that the dual cells are nonconvex, in general. If the polyhedral dual-cell is in the interior of the domain, the interior vertex need not be used as a node but rather only to define the underlying hexahedral cells. The quadrilateral face of each dual cell is planar if the edges of the original tetrahedra are affine. The resulting polyhedral mesh will be referred to as a *type-1* polyhedral-dual mesh. Figure 4 shows the type-1 polyhedral-dual mesh corresponding to the tetrahedral mesh of Fig. 1.

Depending upon the number of attached tetrahedra to a given vertex in the original tetrahedral mesh, the number of vertices of the type-1 dual cell can be quite large, sometimes greater than one hundred. Histograms of element and vertex counts are shown in Fig. 5 for the example shown in Fig. 4. Figure 5a gives the number of attached tetrahedra to vertices in the original tetrahedral mesh. The number of attached tetrahedra exhibits a bimodal distribution with peaks at approximately 12 and 24 attached tetrahedra. The maximum number of attached tetrahedra is 40. Figure 5b gives the number of vertices in the type-1 polyhedral-dual mesh. Most polyhedral elements have between 20 and 80 vertices with a maximum of 120.

3.2. Truncation

The truncation subdivision process consists of two types, full (also called rectification) and partial. The full-truncation subdivision process in two dimensions is illustrated in Fig. 6. Each triangle is first subdivided into four triangles through the introduction of an additional vertex at the midpoint of each edge as shown in Fig. 6a. The rectified triangle corresponds to the interior triangle. Within a patch of elements, a polygonal-dual cell is formed by aggregating the sub-triangles attached to each original triangle vertex as shown in Fig. 6b and Fig. 6c. In three dimensions, each tetrahedron is first subdivided into a 6-vertex octahedron and 4 tetrahedra using edge midpoints as shown in Fig. 2b. Note that each face of the 6-vertex octahedron is a triangle. A polyhedral-dual cell is formed by aggregating the sub-tetrahedra connected to the original tetrahedral vertices. This polyhedral-dual cell will be referred to as a *polytet* element. Examples of the two dual cells (polytet and 6-vertex octahedron) are shown in Fig. 6d. Note that the polytet elements are nonconvex, in general. The resulting polyhedral mesh will be referred to as a *type-2* polyhedral-dual mesh.

Figure 7 shows the type-2 polyhedral-dual mesh corresponding to the tetrahedral mesh of Fig. 1. A histogram of the number of vertices per *polytet* element resulting from the full truncation process is given in Fig. 5c. Most elements have between 5 and 20 vertices.

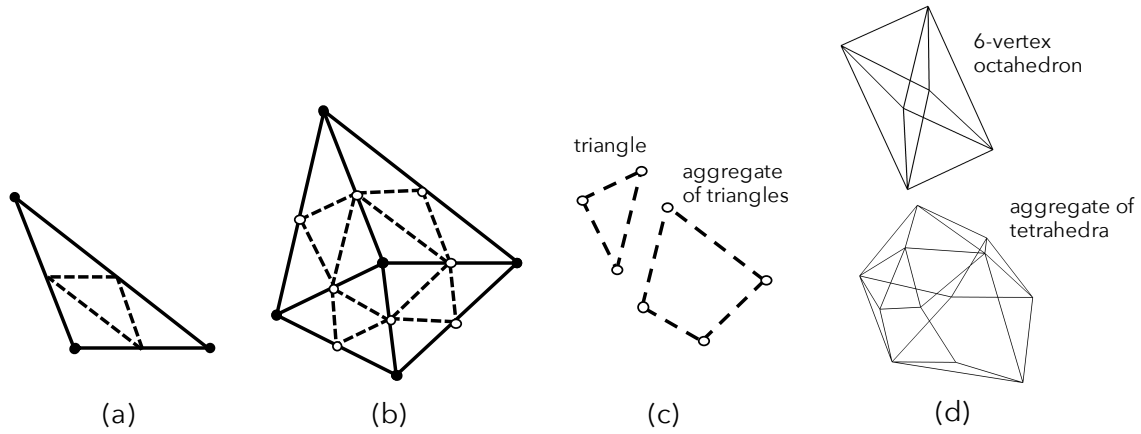

Figure 6: Method of constructing type-2 polyhedral-dual elements using full truncation (rectification). (a) Original triangle and rectification in 2D, (b) triangle patch with rectified triangles, (c) resulting polygonal-dual cell and rectified triangle, and (d) example 6-vertex octahedron (rectified tetrahedron) and a polyhedral-dual cell (polytet) consisting of sub-tetrahedra.

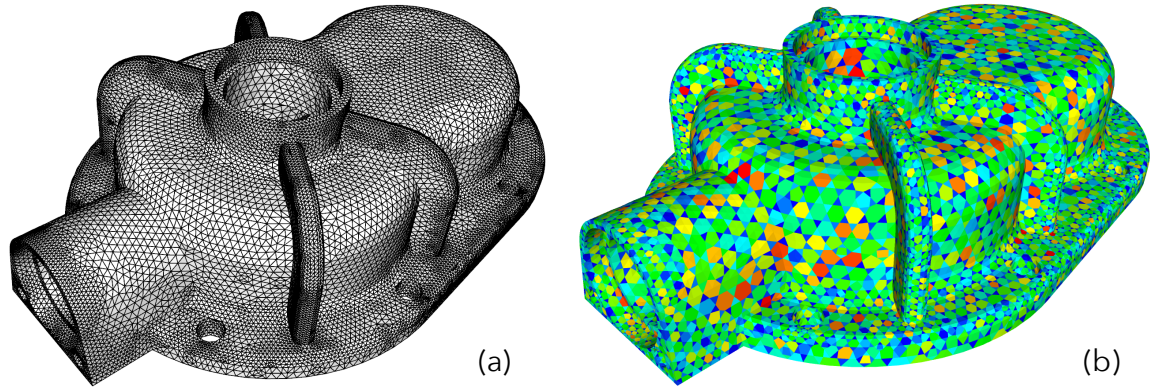

Figure 7: Type-2 polyhedral-dual mesh of the example machine part shown in Fig. 1. (a) Mesh (74,331 vertices, 11,851 polytets (tetrahedral aggregates)), 46,789 6-vertex octahedra) and (b) coloring of elements.

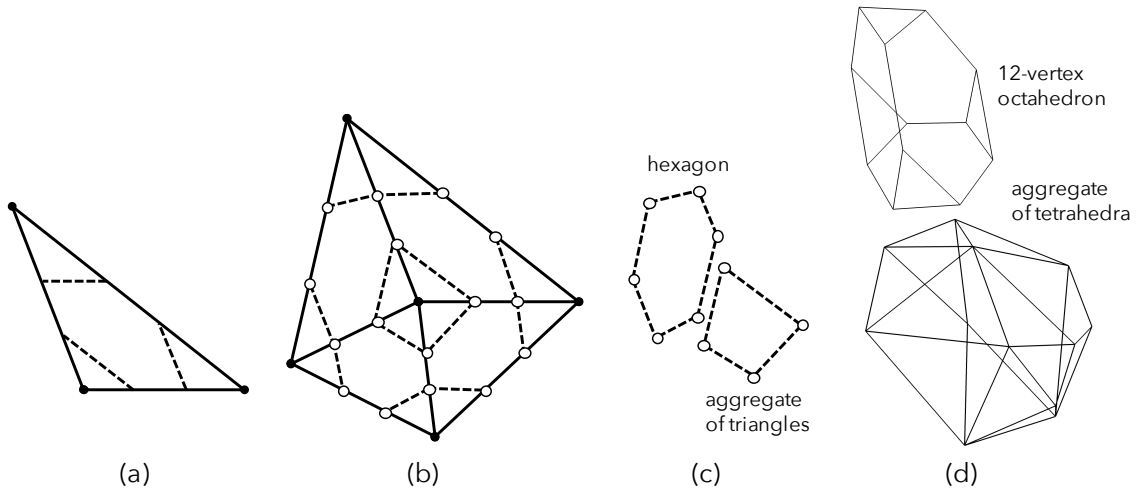

Figure 8: Method of constructing type-3 polyhedral-dual elements using partial truncation. (a) Original triangular element and partial truncation in 2D, (b) triangular patch with partial truncation, (c) new hexagon and polygonal aggregate of triangles, (d) polyhedral aggregate of tetrahedra and 12-vertex octahedron in 3D.

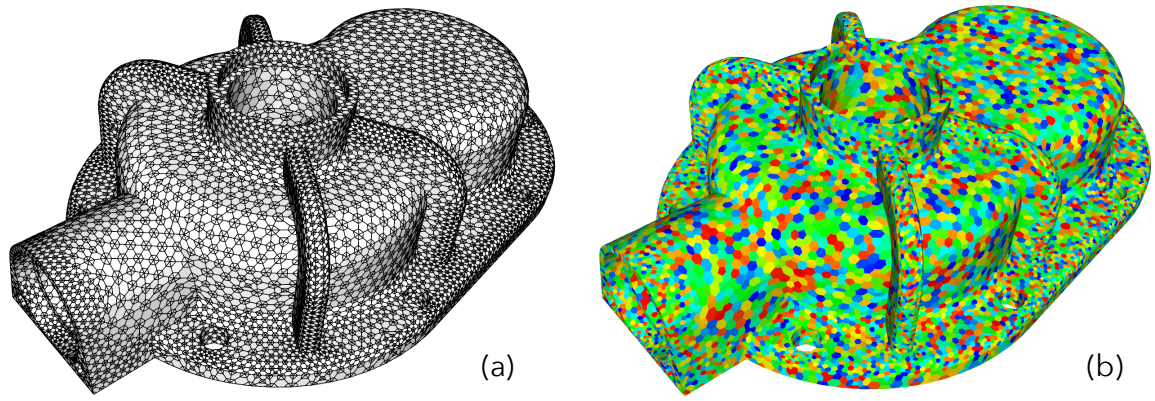

Figure 9: Type-3 polyhedral-dual mesh of the example machine part shown in Fig. 1. (a) Mesh (140, 830 vertices, 11, 851 polytets (tetrahedral aggregates)), 46, 789 12-vertex octahedra) and (b) random coloring of elements.

The partial-truncation subdivision process in two dimensions is illustrated in Fig. 8. Each triangle is first subdivided into three triangles and a hexagon through the introduction of two additional edge vertices as shown in Fig. 8a. The edge subdivisions do not have to be of equal length in general. Here, we only consider an equal-length edge subdivision. As with full-truncation, within a patch of elements a polygonal-dual cell is formed by aggregating the sub-triangles attached to each original triangle vertex as shown in Fig. 8b and Fig. 8c. In three dimensions, each tetrahedron is first subdivided into a 12-vertex octahedron and 4 tetrahedra as shown in Fig. 2c. Note that the faces of this octahedron consist of 4 triangles and 4 hexagons and the hexagonal faces are planar. A polyhedral-dual cell (polytet) is formed by aggregating the sub-tetrahedra connected to the original tetrahedral vertices. Examples of the two dual cells (polytet and 12-vertex octahedron) are shown in Fig. 8d. The resulting polyhedral mesh will be referred to as a *type-3* polyhedral-dual mesh.

Figure 9 shows the type-3 polyhedral-dual mesh corresponding to the tetrahedral mesh of Fig. 1. The histogram of the number of vertices per polytet element remains the same as for the type-2 dual mesh, Fig. 5c.

For simplicity, only the type-3 polyhedral-dual mesh will be considered in the remainder of the paper in the context of finite element analysis. In comparison to the type-1 polyhedral-dual mesh, the type-3 mesh does not have polyhedral elements with a large number of vertices (compare Fig. 5c with Fig. 5b). Also, the 12-vertex octahedron in the type-3 polyhedral mesh is better proportioned to the polytet aggregates than is the 6-vertex octahedron in the type-2 mesh.

4. Polyhedral formulation

In this section, we discuss the finite element formulation for the polyhedral elements resulting from tetrahedral subdivision and aggregation. The element formulation entails the development of element-level shape functions, a consistent integration scheme of the weak form given by (3), and a methodology to avoid locking behavior in the nearly incompressible regime of material behavior. Several formulations are possible. A virtual element formulation, a type of mean-gradient approach (Flanagan and Belytschko, 2015; Cangiani et al., 2015), eliminates the need to define shape functions and naturally provides a consistent integration scheme (Beirão da Veiga et al., 2013; Gain et al., 2014; Chi et al., 2017). However, a virtual element formulation requires artificial stabilization. The choice of stabilization parameters can be problematic for nonlinear applications and for problems with localized contact or concentrated forces (Wriggers et al., 2016). Coarse mesh accuracy can also be effected by the stabilization. Instead, we use an element formulation similar to the one adopted in Bishop (2014). Shape functions are defined on the element, and a first-order integration scheme is used that is sufficient to avoid zero-energy modes. However, the integration scheme does require a correction to the derivatives of the shape-functions in order to obtain a necessary consistency property (Bishop, 2014; Talischi et al., 2015).

4.1. Shape functions

Due to the geometric structure of the polyhedral-dual meshes (e.g., the polyhedral elements have planar faces), several types of shape functions may be used (Sukumar and Malsch, 2006; Wicke et al., 2007; Hormann and Sukumar, 2018). For example, Wachspress shape functions could be used for the 12-vertex octahedra, since the elements are convex and have planar faces (Wachspress, 1975). Both max-ent and harmonic shape functions could also be used for any of the element types (Sukumar, 2004; Joshi et al., 2007; Martin et al., 2008; Hormann and Sukumar, 2008; Bishop, 2014). Both max-ent and harmonic shape functions are strictly positive, although the approximate solution for harmonic shape functions can result in small violations of the positivity property. For simplicity, only harmonic and max-ent shape functions are considered here.

The shape functions $\psi_a(\boldsymbol{X}), a = 1, \ldots, N_{\mathrm{v}}$, are defined directly on the initial configuration of the element. There is no mapping to a parent coordinate system as with standard finite elements (Hughes, 2000). The integration of the weak form of the governing equations (Section 2.3) is also performed directly on the initial configuration of the element as described in Section 4.2.

4.1.1. Harmonic shape functions

Harmonic functions minimize the Dirichlet energy given by the following functional

$$J(\psi) := \frac{1}{2} \int_{\Omega_{\mathrm{e}}} \nabla\psi \cdot \nabla\psi \; d\boldsymbol{X} \tag{4}$$

with $\psi \in H^1(\Omega_{\mathrm{e}})$. The minimizer of this functional satisfies the following variational problem: find $\psi \in H^1(\Omega_{\mathrm{e}})$ with $\psi = \overline{\psi}$ on Γ_{e} such that

$$\int_{\Omega_{\mathrm{e}}} \nabla\psi \cdot \nabla v \; d\boldsymbol{X} = 0 \tag{5}$$

for all test functions $v \in H^1_0(\Omega_{\mathrm{e}})$. The strong form of this variational problem is simply,

$$\nabla^2\psi = 0 \;\text{ in }\; \Omega_{\mathrm{e}} \quad \text{with} \quad \psi = \overline{\psi} \;\text{ on }\; \Gamma_{\mathrm{e}} \,. \tag{6}$$

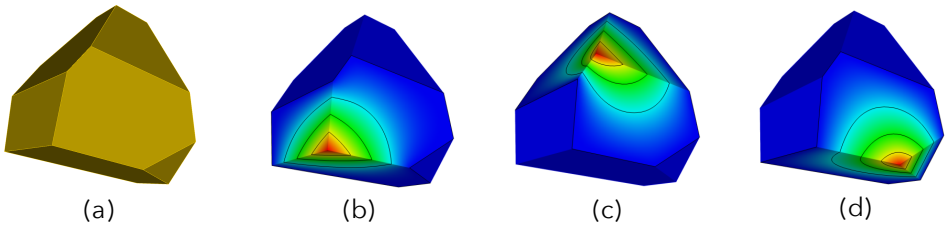

Figure 10: (a) Example polyhedron with element shape functions shown for three vertices (b)–(d). (Adapted from Bishop (2014).)

Boundary conditions for each shape function are prescribed such that the resulting shape functions naturally form a partition of unity,

$$\sum_{a=1}^{N_\mathrm{v}} \psi_a(\boldsymbol{X}) = 1 \tag{7}$$

and linear reproducibility

$$\sum_{a=1}^{N_\mathrm{v}} \psi_a(\boldsymbol{X})\, \boldsymbol{X}_a = \boldsymbol{X}. \tag{8}$$

The appropriate boundary conditions are described in Joshi et al. (2007); Martin et al. (2008); Bishop (2014). The property of linear reproducibility, together with a consistent integration scheme presented in the next section, result in an isoparametric first-order finite element formulation with optimal rates of convergence.

Example shape functions are shown in Fig. 10. By construction, the harmonic shape functions possess the Kronecker-delta property at the nodes. This property simplifies the enforcement of displacement boundary conditions in the finite element solution. Note that while the shape functions are shown for the entire element in Fig. 10, only their values and derivatives at the quadrature points need to be determined. In Bishop (2014), solutions to (5) were approximated using the finite element method on a sub-tetrahedral mesh of the element. The construction of this sub-tetrahedral mesh was obtained by assuming that the element shape was star-convex with respect to the vertex-averaged centroid. For a polyhedral-dual mesh, the 6-vertex and 12-vertex polyhedra are strictly convex and thus the method of Bishop (2014) can be used to solve (6). Also, for the polytet elements, the sub-tetrahedra naturally provide a mesh on which to solve (6). It was proven in Bishop (2014) that shape functions obtained using finite element approximations of (6) also possess the linear reproducing properties, (7) and (8).

A necessary condition on the shape function derivatives for passing the patch test (see Section 5.1) is obtained by taking the gradient of (7) and (8) (Krongauz and Belytschko, 1997), resulting in

$$\sum_{a=1}^{N_\mathrm{v}} \nabla\psi_a(\boldsymbol{X}) = 0\,, \quad \sum_{a=1}^{N_\mathrm{v}} \nabla\psi_a(\boldsymbol{X}) \otimes \boldsymbol{X}_a = \boldsymbol{I}\,, \quad \boldsymbol{X} \in \Omega_\mathrm{e}\,. \tag{9}$$

4.1.2. Maximum entropy shape functions

The max-ent shape functions involve the formulation of a convex optimization problem in terms of a relative entropy functional with linear reproducing constraints (Sukumar, 2004; Arroyo and Ortiz, 2006; Sukumar and Wright, 2007; Hormann and Sukumar, 2008). For a given $\boldsymbol{X} \in \Omega_\mathrm{e}$, the shape functions $\psi_a(\boldsymbol{X}), a = 1, \ldots, N_\mathrm{v}$, are found by minimizing the functional

$$J(\psi_a, a = 1, \ldots N_\mathrm{v}) := \sum_{a=1}^{N_\mathrm{v}} \psi_a(\boldsymbol{X})\, \ln\left(\frac{\psi_a(\boldsymbol{X})}{w_a(\boldsymbol{X})}\right) \tag{10}$$

subject to the reproducing constraints, (7) and (8). Here, $w_a(\boldsymbol{X})$ is a suitable *prior* weight function for the given vertex. This constrained optimization problem can be solved using the method of Lagrange multipliers.

Following Sukumar and Wright (2007), the Lagrangian $\mathcal{L}(\psi_a, \lambda_0, \boldsymbol{\lambda})$ is defined as

$$\mathcal{L}(\psi_a, \lambda_0, \boldsymbol{\lambda}) := \sum_{a=1}^{N_\mathrm{v}} \psi_a(\boldsymbol{X}) \, \ln\left(\frac{\psi_a(\boldsymbol{X})}{w_a(\boldsymbol{X})}\right) + \lambda_0 \left(\sum_{a=1}^{N_\mathrm{v}} \psi_a(\boldsymbol{X}) - 1\right) + \boldsymbol{\lambda} \cdot \left(\sum_{a=1}^{N_\mathrm{v}} \psi_a(\boldsymbol{X}) \, \boldsymbol{X}_a - \boldsymbol{X}\right) \tag{11}$$

where λ_0 and $\boldsymbol{\lambda}$ are the Lagrange multipliers associated with the constraints for partition of unity and linear precision, respectively. The first-order optimality conditions and the subsequent solution for $\psi_a(\boldsymbol{X})$ are discussed in detail in Arroyo and Ortiz (2006); Sukumar and Wright (2007). Examples of the max-ent shape functions on both convex and nonconvex polygons are given in Sukumar (2004); Hormann and Sukumar (2018). Construction of the derivatives of the max-ent shape functions is discussed in Sukumar and Wright (2007). The max-ent shape functions require an iterative solution (e.g. Newton's method), but only need to be obtained at the quadrature points of the element as described in Section 4.2.

4.2. Consistent element integration

Nonlinear computational solid mechanics typically involves the use of numerically expensive constitutive models, e.g., those with internal-state variables (de Souza Neto et al., 2008). For an explicit time-integration scheme, the element is integrated at every time step in order to assemble the internal-force vector. Thus, it is imperative to minimize the number of quadrature points, while avoiding the use of an integration scheme that would result in a zero or low-energy mode. In Rashid and Selimotic (2006), an integration scheme is used in which the number of quadrature points is equal to the number of element vertices. In this approach, a polyhedron is partitioned into N_v tributary regions with each region associated with a vertex. A quadrature point is placed at the centroid of each tributary region, and the quadrature weight is simply the volume of the tributary region. This integration scheme has only linear precision (can integrate linear functions exactly), but is sufficient to guarantee convergence of the overall finite element formulation. This approach was also used by Bishop (2014). For the present application, we use the integration scheme of Rashid and Selimotic (2006) only for the octahedral elements (both 12-vertex and 6-vertex). For the polytet elements, consisting of an aggregate of tetrahedra, we simply place one quadrature point at each centroid of the tetrahedron. Numerical experiments confirmed that this element integration scheme (for polytet elements) was sufficient to avoid zero or low-energy modes, although more investigation is needed.

Since the harmonic and max-ent shape functions are nonpolynomial in nature, significant error is introduced with the use of a first-order integration scheme. This error ultimately results in a failure to pass the patch test (a test for polynomial completeness in the element formulation) as demonstrated in Section 5.1. To circumvent this difficulty, the derivatives of the shape functions must be modified to satisfy the discrete divergence theorem while maintaining other necessary consistency properties. This derivative correction restores the so-called *integration consistency* identified by Krongauz and Belytschko (1997) and applied in the context of meshfree methods by Chen et al. (2001) and polyhedral finite elements by Bishop (2009, 2014); Talischi et al. (2015). The divergence theorem states that

$$\int_{\Omega_\mathrm{e}} \nabla\psi_a \, d\boldsymbol{X} = \int_{\Gamma_\mathrm{e}} \psi^a \, \boldsymbol{N} \, dS \tag{12}$$

where $\boldsymbol{N}$ is the outward unit normal vector on Γ_e. In discrete form, this becomes

$$\sum_{k=1}^{N_\mathrm{Q}} w_k \nabla\psi_{ak} = \sum_{l=1}^{N_\mathrm{Q}^\Gamma} w_l^\Gamma \, \psi_{al} \, \boldsymbol{N}_l \,, \quad (a = 1, \ldots, N_\mathrm{v}) \tag{13}$$

where $\psi_{ak} := \psi_a(\boldsymbol{X}_k)$, and $\boldsymbol{X}_k$ is the position of the k-th quadrature point. The quadrature weight is w_k in the element volume and w_l^Γ on the element surface (faces). The number of quadrature points in the element volume is N_Q, and the number of quadrature points on the element surface is N_Q^Γ. For nonpolynomial shape functions, (13) will not be satisfied in general, yet satisfaction of this identity is critical to pass the patch test.

In order to satisfy this integration constraint, we slightly modify the derivatives of the shape functions (a derivative correction). This derivative correction is obtained by minimizing the weighted sum of the squared differences with respect to the original values subject to the constraint (13):

$$\min_{\boldsymbol{\xi}_k \in \boldsymbol{R}^3} \sum_{k=1}^{N_\mathrm{Q}} w_k ||\boldsymbol{\xi}_k - \nabla \psi_{ak}||^2 \tag{14}$$

subject to the constraint

$$\sum_{k=1}^{N_\mathrm{Q}} w_k \, \boldsymbol{\xi}_k - \sum_{l=1}^{N_\mathrm{Q}^\Gamma} w_l^\Gamma \psi_{al} \boldsymbol{N}_l = 0 \,. \tag{15}$$

Let $\boldsymbol{d}_{ak}$ represent the solution of this constrained minimization problem for each shape function ψ_a and quadrature point $\boldsymbol{X}_k$. This problem is solved for each shape function and coordinate direction, independently, using the method of Lagrange multipliers (Luenberger, 2003, Ch. 10). This constrained minimization problem differs slightly from that used in Bishop (2009, 2014) by the inclusion of the quadrature weights w_k in (14). Numerical tests have shown only small differences between the two approaches. The Lagrangian $\mathcal{L}$ associated with the constrained problem is defined as

$$\mathcal{L}(\boldsymbol{\xi}_k, \boldsymbol{\lambda}) := \sum_{k=1}^{N_\mathrm{Q}} w_k ||\boldsymbol{\xi}_k - \nabla \psi_{ak}||^2 + \boldsymbol{\lambda} \cdot \left(\sum_{k=1}^{N_\mathrm{Q}} w_k \, \boldsymbol{\xi}_k - \sum_{l=1}^{N_\mathrm{Q}^\Gamma} w_l^\Gamma \psi_{al} \boldsymbol{N}_l \right) \tag{16}$$

where $\boldsymbol{\lambda}$ is the Lagrange multiplier vector. The necessary conditions for a local minimum are given by

$$\frac{\partial L}{\partial \boldsymbol{\xi}_k} = 0 \quad (k = 1, \ldots, N_\mathrm{Q}) \,. \tag{17}$$

Surprisingly, this procedure for modifying the shape-function derivatives does not corrupt their consistency properties given in (9). A proof of this result was given in Bishop (2014) for the case when the quadrature weights in (14) are not included. The proof still holds when the quadrature weights are included. The updated proof is given in Appendix A.

4.3. Near incompressibility

To prevent locking behavior in the nearly incompressible regime, a mean-dilation approach is used, commonly referred to as B-bar in the linear regime (Hughes, 2000, Ch. 4.5) and F-bar in the large-deformation regime (de Souza Neto et al., 2008, Ch. 15). The examples shown in Section 6 demonstrate the performance of these approaches in nearly incompressible regime including elasto-plasticity.

4.4. Explicit dynamics

For high-rate phenomena, (3) is typically integrated using a central-difference explicit-time integration scheme (Belytschko et al., 2014, Ch. 6). To obtain a diagonalized mass matrix for a polyhedral mesh, the special lumping technique of Hinton et al. (1976) is used. This mass lumping procedure is recommended by Hughes for non-standard element formulations as it is guaranteed to produce positive lumped masses. This approach was used by Bishop (2009) for modeling pervasive fracture phenomena with random polygonal meshes and more recently by Bishop et al. (2016); Chin et al. (2018).

5. Verification

In this section, several verification examples are presented. The engineering patch test is discussed in Section 5.1. Convergence results are reported for a three-dimensional linear elastic beam in both bending and torsional loadings in Sections 5.2 and 5.3, respectively. The convergence behavior in the nearly incompressible regime is explored using the B-bar formulation in Section 5.4. The behavior in the nearly incompressible regime is studied further in Section 5.5 using the Cook's membrane problem.

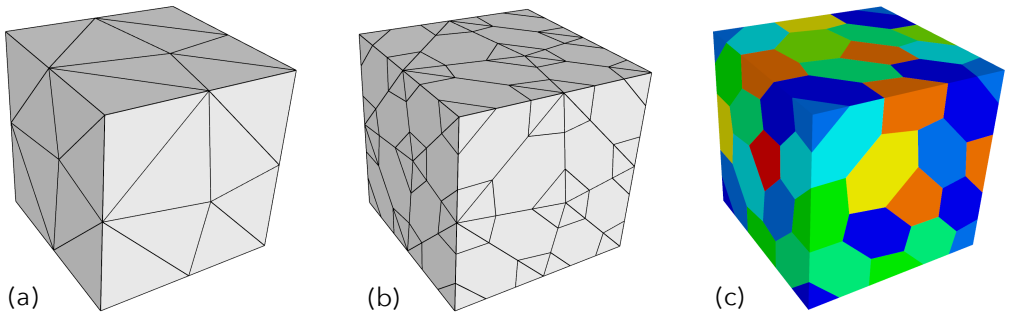

Figure 11: Polyhedral mesh of a cube for use in the patch-test verification problem. (a) tetrahedral mesh (29 nodes, 59 tetrahedra), (b) type-3 polyhedral-dual mesh (248 nodes, 29 polytet, 59 octahedra), and (c) random coloring of elements.

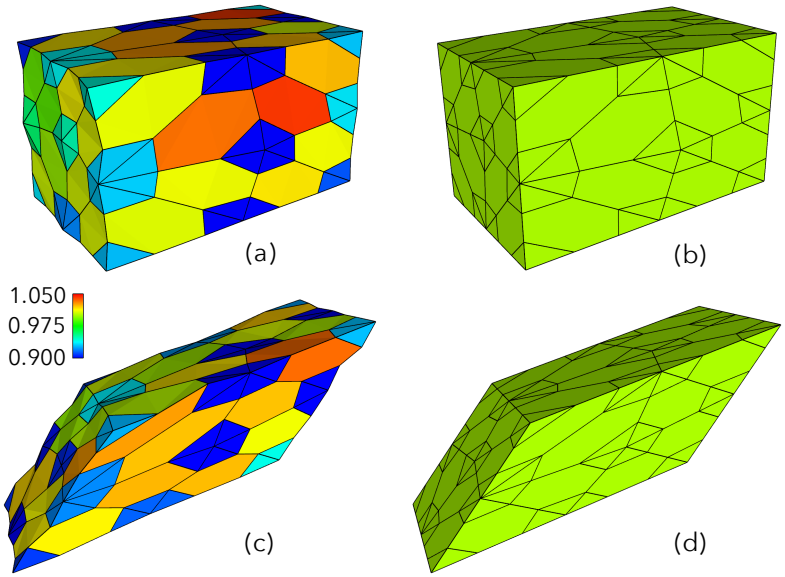

Figure 12: Results for the patch-test verification problem without (a), (c) and with (b), (d) correction of the shape function derivatives to satisfy integration consistency: (a), (b) uniaxial tension, $\sigma_{11} = 1.0$, (c), (d) pure shear, $\sigma_{12} = 1.0$.

5.1. Patch test

The patch test is commonly used to test new finite element formulations for polynomial completeness up to a given order (Hughes, 2000; Belytschko et al., 2014). For first-order elements presented here, a small collection of elements (a patch) is verified to reproduce linear polynomials. The patch test consists of applying uniform tractions to the boundary, and then verifying that the resulting finite element solution returns the exact linear displacement field. Equivalently, displacement boundary conditions corresponding to the exact displacement field for a uniform stress state can be applied. For the present series of patch tests, a cubical domain is used as shown in Fig. 11. The material is taken to be isotropic and linear eleastic with a Young's modulus of 1.0 and a Poisson's ratio of 0.3. Tractions corresponding to a stress field with only one nonzero component and with a unit value are applied to the patch. This test is repeated for each of the six stress components.

Figure 12 shows results for two of the patch tests, a uniaxial loading (a), (b) and a pure shear loading (c), (d), using harmonic shape functions. The displacements are scaled by a factor of 0.5 for clarity. Results are provided both without (a), (c) and with (b), (d) correction of the shape function derivatives for integration consistency. The patch test is clearly violated without the correction of the derivatives. The stress error for

Table 1: Stress error (maximum) in the patch test over all stress components, without and with correction of the shape function derivatives to satisfy integration consistency (see Fig. 12).

applied traction state	without correction	with correction
tension	0.18	$9.6 \cdot 10^{-13}$
shear	0.13	$2.7 \cdot 10^{-12}$

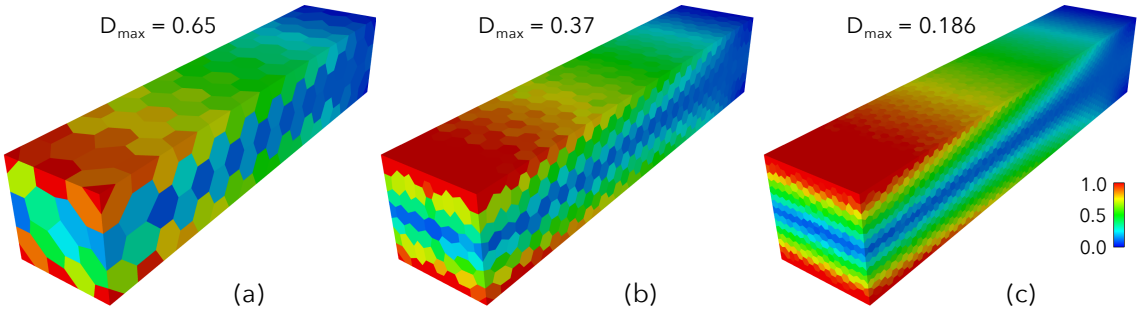

Figure 13: von Mises stress field for the verification problem of a three-dimensional beam in bending under a transverse shear load at three levels of mesh refinement. The maximum element diameter D_{max} is given.

these tests is given in Table 1. Results using max-ent shape functions are similar.

5.2. Three-dimensional linear elastic beam in bending with shear

For the next verification test, we consider a linear elastic prismatic beam in bending under a transverse shear load. The material is taken to be isotropic and linear elastic with a Young's modulus of 1.0 and a Poisson's ratio of 0.3. The beam has a square cross section and length to width ratio of five. The exact stress solution is provided by Barber (2010) and displacement field by Bishop (2014). The exact displacements were enforced on one end of the beam, while tractions were applied to the other end. A sequence of refined tetrahedral meshes was created along with type-3 polyhedral-dual meshes. The von Mises stress field for three mesh refinements using harmonic shape functions are shown in Fig. 13.

Convergence results are shown in Fig. 14 in both the L_2 norm and energy semi-norm. The rates of convergence are close to the theoretical convergence values of 2.0 and 1.0, respectively. Results for both harmonic and max-ent shape functions are provided. The max-ent shape functions were used only for the polytet aggregate elements. There is very little difference between results using the two different types of shape functions. Similar small differences have been observed in a meshfree context by (Bishop, 2019) when comparing the approximability of extreme deformation fields using both max-ent and reproducing-kernel basis functions. The differences may be larger if the max-ent shape functions were also used in the 12-vertex octahedra. These results are consistent with the small differences in polygonal shape functions shown in (Hormann and Sukumar, 2018, Ch. 1) for both convex and nonconvex elements.

5.3. Three-dimensional linear elastic beam in torsion

For the next verification test, we consider the same three-dimensional linear elastic prismatic beam but instead with torsional loading. The exact stress solution is provided by Barber (2010) and displacement field by Bishop (2014). The exact displacements were enforced on one end of the beam, while tractions were applied to the other end. The von Mises stress field for three mesh refinements using harmonic shape functions are shown in Fig. 15. Convergence results are given in Fig. 16 in both the L_2 norm and energy semi-norm. As with the bending case, the rates of convergence are close to the theoretical convergence values. Again, there is very little difference between results using the harmonic and max-ent shape functions.

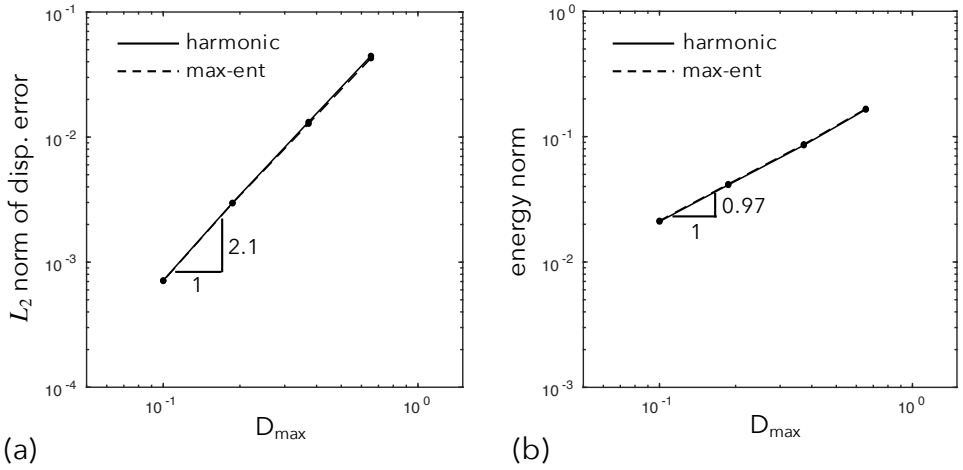

Figure 14: Convergence results for the verification problem of a three-dimensional beam in bending under a transverse shear load. (a) L_2 norm of displacement error and (b) energy semi-norm of displacement error. Results are shown for both harmonic and maximum-entropy shape functions (polytet aggregate elements only). Rates of convergence are identified. (Poisson's ratio is 0.3; $D_{\max}$ is the maximum element diameter.)

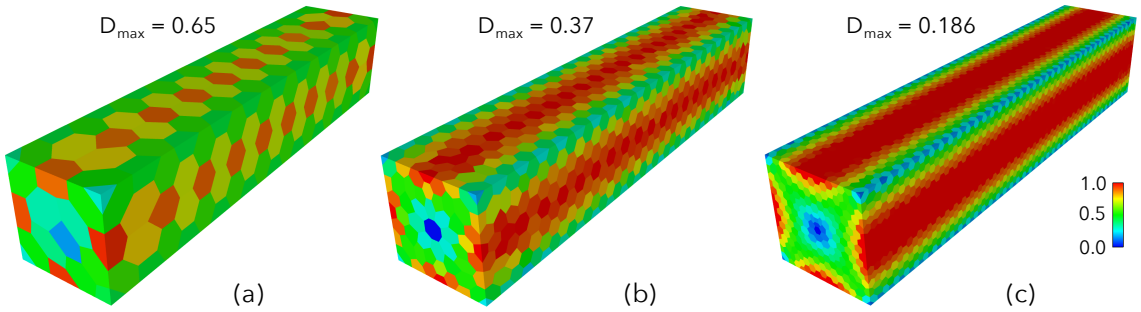

Figure 15: von Mises stress field for the verification problem of a three-dimensional beam in torsion at three levels of mesh refinement in the initial tetrahedral mesh. The maximum element diameter is given.

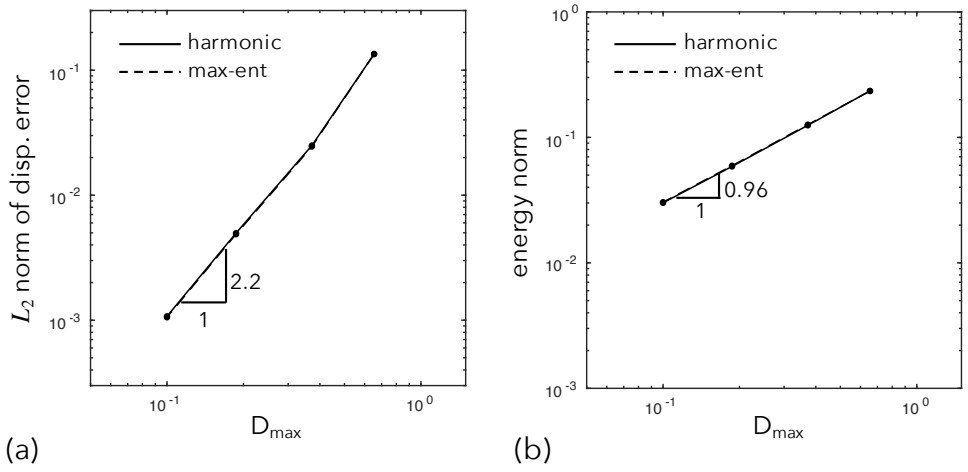

Figure 16: Convergence results for the verification problem of a three-dimensional beam in torsion. (a) L_2 norm of displacement error and (b) energy semi-norm of displacement error. Results are show for both harmonic and maximum-entropy shape functions (polytet aggregate elements only). Rates of convergence are identified. (Poisson's ratio is 0.3, $D_{\max}$ is the maximum element diameter.)

5.4. Three-dimensional nearly incompressible linear elastic beam

For the next verification test, we explore the behavior of the polyhedral-dual elements in the nearly incompressible regime (Poisson's ratio $\nu \to 0.5$) using the B-bar formulation and harmonic shape functions. We consider the same three-dimensional beam and loading presented in Section 5.2. Convergence results are given in Fig. 17 in both the L_2 norm and energy semi-norm for several values of Poisson's ratio. There is no observed degradation in coarse-mesh accuracy or convergence rate.

5.5. Cook's membrane, nearly incompressible

For the final verification test, we consider the Cook's membrane problem in the nearly incompressible regime using the B-bar formulation. The Cook's membrane problem is commonly used to explore the behavior of finite element formulations in the nearly incompressible regime undergoing a mixture of shear and bending strains (Korelc and Wriggers, 1996; Ostien et al., 2016). The boundary-value problem is shown in Fig. 18. The domain consists of the quadrilateral ABCD. The edge AD is fixed while a shear traction T is applied to edge BC. Plane strain conditions are enforced through the thickness of the plate (Z-direction) by prescribing $u_3 = 0$. The material is taken to be isotropic and linear elastic with a Young's modulus of 1.0 and a Poisson's ratio of 0.4999.

A coarse polyhedral-dual mesh for the domain is shown in Fig. 19. A conventional hexahedral mesh is also shown. A finer mesh is also used with approximately one-half of the maximum-element size. A comparison of pressure fields from Cook's membrane verification problem using coarse (a), (b) and fine (c), (d) polyhedral-dual meshes is shown in Fig. 20 using both the standard formulation (a), (c) and B-bar formulation (b), (d). The pressure field is smooth for the B-bar formulation, but the solution is unstable showing a highly oscillatory pressure field when using the standard formulation. Results using a conventional trilinear hexahedral element are shown in Fig. 21 for comparison. Interestingly, there is severe locking for the standard formulation, but still exhibits some locking behavior for the B-bar formulation, whereas this is not observed in the polyhedral formulation.

6. Examples

In this section, several nonlinear examples are presented using the type-3 polyhedral mesh. Results are also provided using conventional hexahedral elements for comparison. In Section 6.1, a hyperelastic I-beam is subjected to torsion and large deformation. Section 6.2 shows the response of an elastic-plastic plate

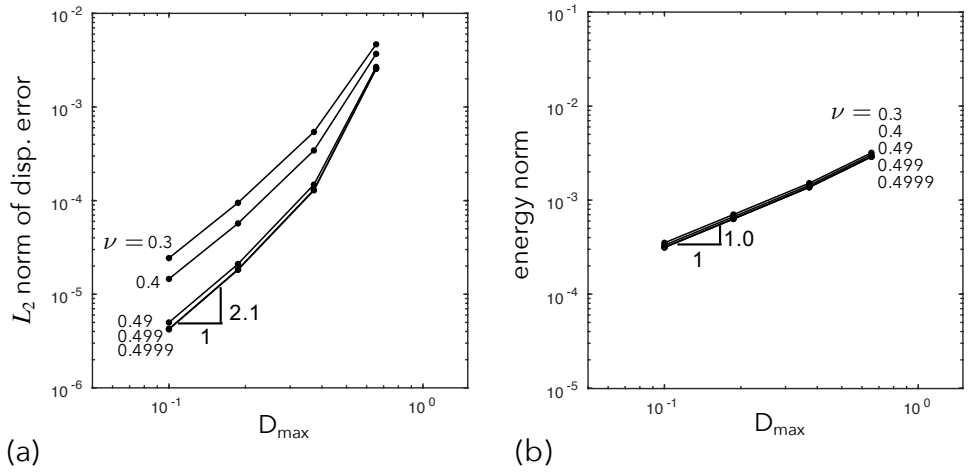

Figure 17: Convergence results for the verification problem of a three-dimensional beam in bending with transverse shear load for various values of Poisson's ration ν approaching the incompressible limit of $\nu = 0.5$ using the B-bar formulation. (a) L_2 norm of displacement error and (b) energy semi-norm of displacement error. Rates of convergence are identified. ($D_{\max}$ is the maximum element diameter.)

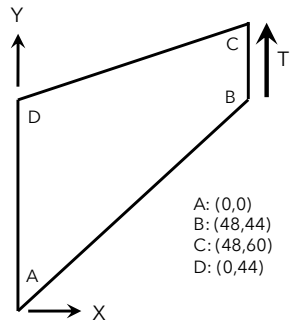

Figure 18: Definition of the domain for the Cook's membrane verification problem. The edge AD is fixed while a shear traction T is applied to edge BC. Plane strain conditions are enforced through the thickness of the plate.

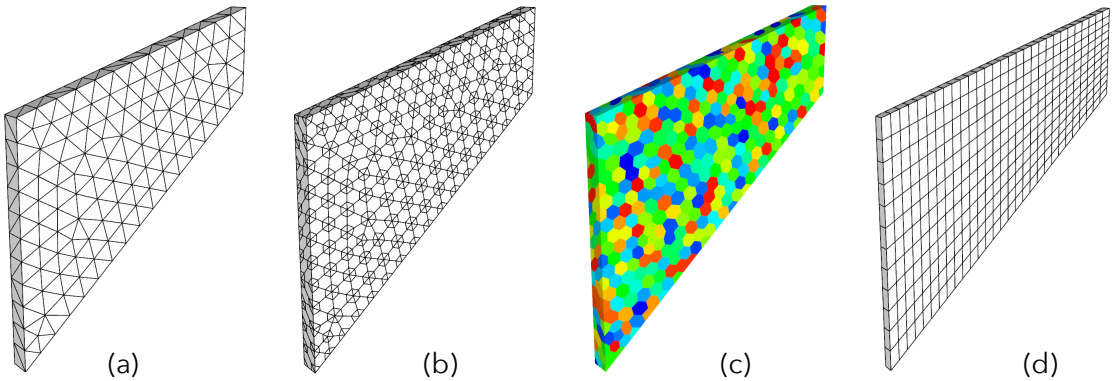

Figure 19: Type-3 polyhedral-dual mesh of the Cook's membrane verification problem. (a) Coarse tetrahedral mesh (270 nodes, 758 tetrahedra), (b) type-3 polyhedral-dual mesh (2, 788 nodes, 270 polytet, 758 octahedra), (c) random coloring of elements, and (d) a conventional hexahedral mesh (780 nodes, 348 hexahedra).

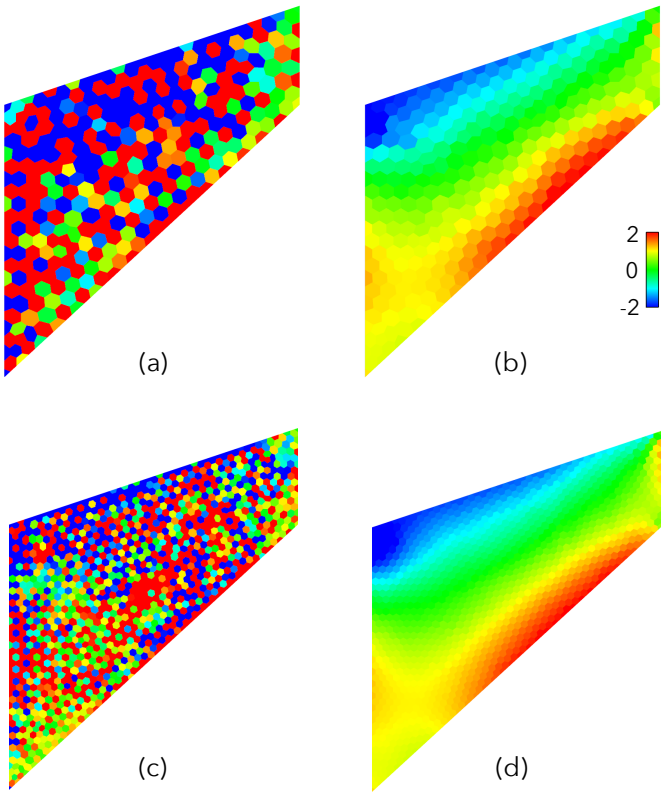

Figure 20: Comparison of pressure fields from Cook's membrane verification problem using coarse (a), (b) and fine (c), (d) type-3 polyhedral-dual meshes with a Poisson's ratio of 0.4999. (a), (c) standard formulation, (b), (d) B-bar formulation.

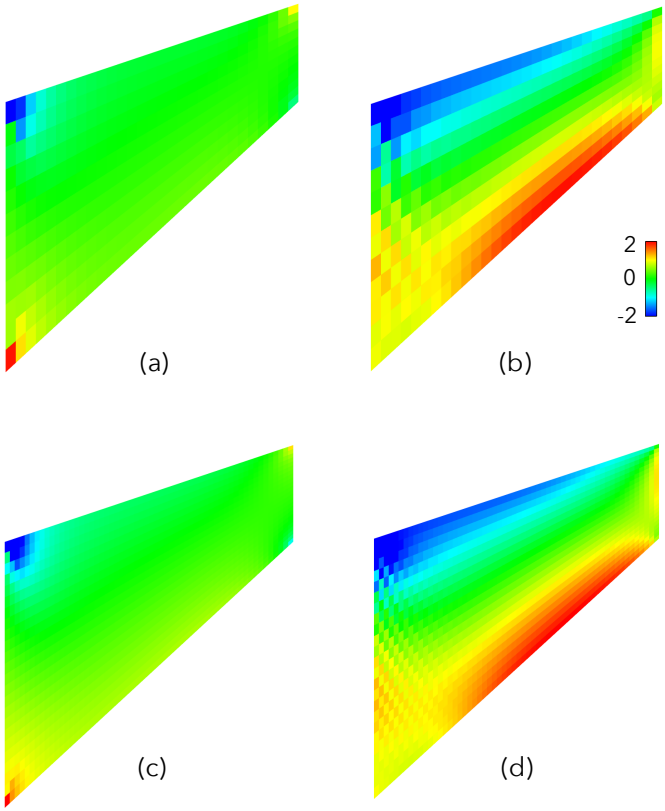

Figure 21: Comparison of pressure fields from Cook's membrane verification problem using coarse (a), (b) and fine (c), (d) hexahedral meshes with a Poisson's ratio of 0.4999. (a), (c) standard formulation, (b), (d) B-bar formulation.

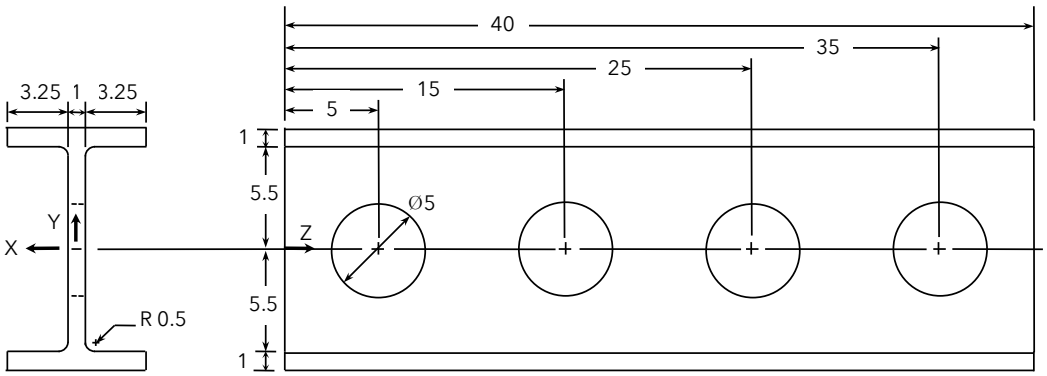

Figure 22: Geometry definition for the I-beam example problem.

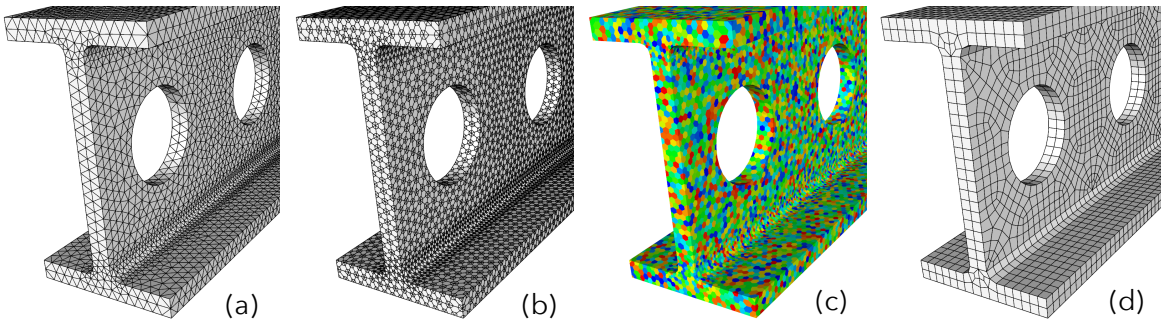

Figure 23: Polyhedral mesh of the I-beam example problem. (a) Initial tetrahedral mesh (25,598 nodes, 117,436 tetrahedra), (b) type-3 polyhedral-dual mesh (321,783 nodes, 25,598 polytet, 117,436 octahedra), (c) random coloring of elements, and (d) a conventional coarse hexahedral mesh (13,137 nodes, 8,576 hexahedra).

containing a hole subjected to uniaxial extension. The Taylor-bar impact problem is presented in Section 6.3. Finally, in Section 6.4, a linear elastic analysis of the machine part used in Section 3 is presented.

The Cubit meshing software was used to create the initial tetrahedral mesh as well as reference hexahedral meshes (Cubit, 2018). For the nonlinear example problems, the explicit-dynamics time-integration scheme described in Section 4.4 was used. The critical time step was calculated using the dilational wave speed and the minimum edge length over all elements in the deformed mesh. The resulting characteristic time was scaled by a factor of 0.7 in order to achieve a stable time step.

6.1. Hyperelastic I-beam in torsion

For a first nonlinear example using a polyhedral-dual mesh, we consider the large-deformation response of a hyperelastic I-beam subjected to a torsional load. The geometry definition is given in Fig. 22. A polyhedral-dual mesh for the domain is shown in Fig. 23. A coarse hexahedral mesh is also shown. A refined hexahedral mesh (uniform 1 to 8 refinement) is used to provide a comparison to the results obtained using the polyhedral-dual mesh.

The constitutive model is taken be neo-Hookean hyperelastic with a Young's modulus of 100 GPa and a Poisson's ratio of 0.3 (Bonet and Wood, 2008, Ch. 6.4). The beam is fixed on one end while the other end is prescribed a pure rotation through 90 degrees. The axial motion is constrained at both ends. The prescribed motion is quasistatic.

The deformed configuration of the I-beam is shown in Fig. 24 for both the polyhedral-dual mesh and the refined hexahedral mesh after a 90 degree rotation. The von Mises stress field is also shown. The stress field was not post-processed (smoothed). The deformation and stress fields are nearly identical. The axial

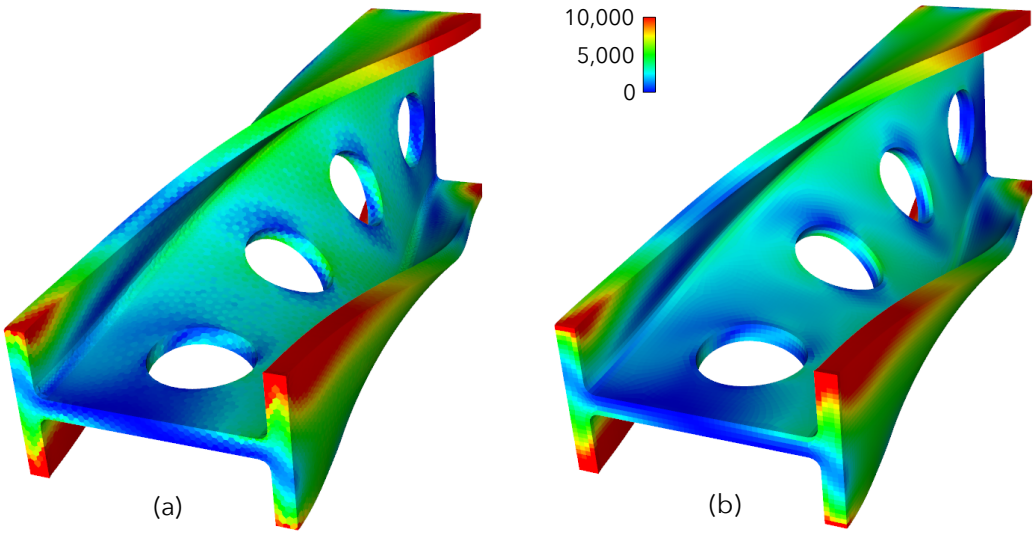

Figure 24: Comparison of the von Mises stress field in a hyperelastic I-beam subjected to a large torsional rotation using both (a) polyhedral dual and (b) hexahedral discretizations. (Stress units are MPa.)

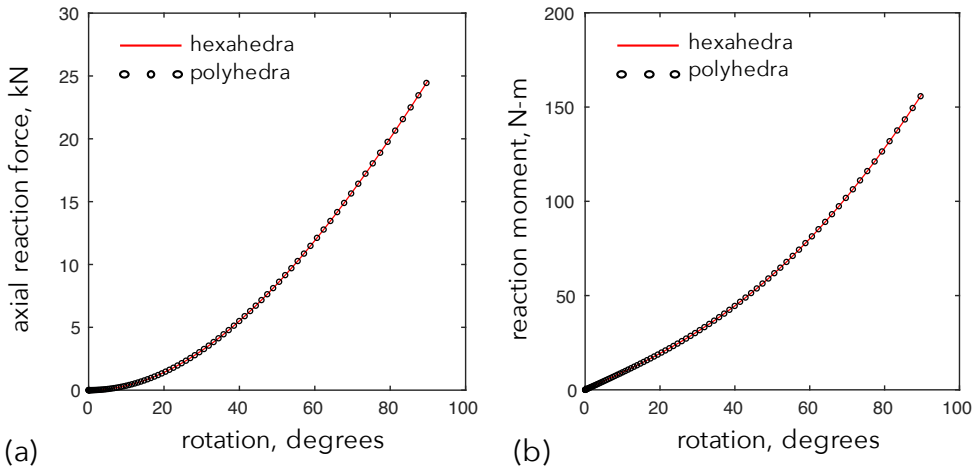

Figure 25: Comparisons of (a) reaction force and (b) moment of a hyperelastic I-beam subjected to a large torsional rotation using both polyhedral dual and hexahedral discretizations.

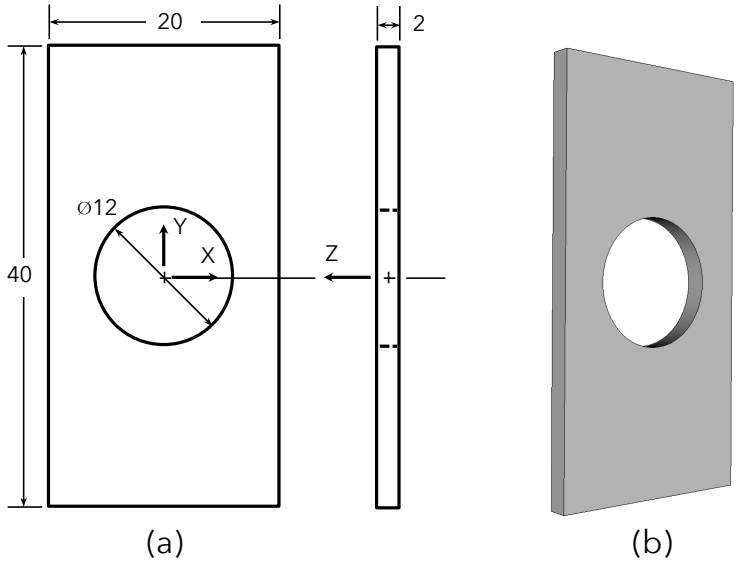

Figure 26: (a) Geometry definition and (b) three-dimensional view for the problem of a plate with hole.

force and moment reactions are shown in Fig. 25 for both the polyhedral-dual mesh and hexahedral mesh. The reactions are nearly identical.

6.2. Elastic-plastic deformation of a plate with hole

For the next example, we consider the elasto-plastic response of a plate with hole subjected to uniform axial extension. The geometry definition is given in Fig. 26. A polyhedral-dual mesh for the domain is shown in Fig. 27. A coarse hexahedral mesh is also shown. A refined hexahedral mesh (two stages of uniform 1 to 8 refinement) is used to provide a comparison to the results obtained using a polyhedral-dual mesh.

An isotropic large-strain elasto-plastic constitutive model is used. The model follows Eterovic and Bathe (1990) with further elaboration (and corrections) by (Bathe, 1996, Ch. 6.6.4). Young's modulus and Poisson's ratio are take to be 100 GPa and 0.3, respectively. The yield stress is taken to be 300 MPa with a hardening modulus of 500 MPa. The hardening is taken to be isotropic.

The plate is subjected to uniform extension. The prescribed motion is quasistatic. The deformed configuration of the plate is shown in Fig. 28 at an extension of 2 mm. The hydrostatic stress field, von Mises stress field, and equivalent plastic strain are shown. The stress field was not post-processed (smoothed). The deformed configuration with stress fields obtained using the refined hexahedral mesh are shown in Fig. 29. The deformation and stress fields are nearly identical. The axial reaction force is shown in Fig. 30 for both the polyhedral-dual mesh and hexahedral mesh. The reaction force is nearly identical.

6.3. Taylor-bar impact

For the next example, we consider the Taylor-bar impact problem consisting of a small cylinder impacting a rigid surface (Taylor, 1948). The cylinder has a height of 24 mm and a diameter of 8 mm. A polyhedral-dual mesh for the domain is shown in Fig. 31. A coarse hexahedral mesh is also shown. A refined hexahedral mesh (uniform 1 to 8 refinement) is used to provide a comparison to the results obtained using a polyhedral-dual mesh.

The elasto-plastic material model used for the previous example (Section 6.2) is also used here. The density of the material is taken to be 2700 kg/m^3. The impact velocity of the cylinder is 300 m/s. To model the impact, the nodes on the impact face are prescribed both zero displacement and velocity in the axial direction. Loss of contact is not modeled.

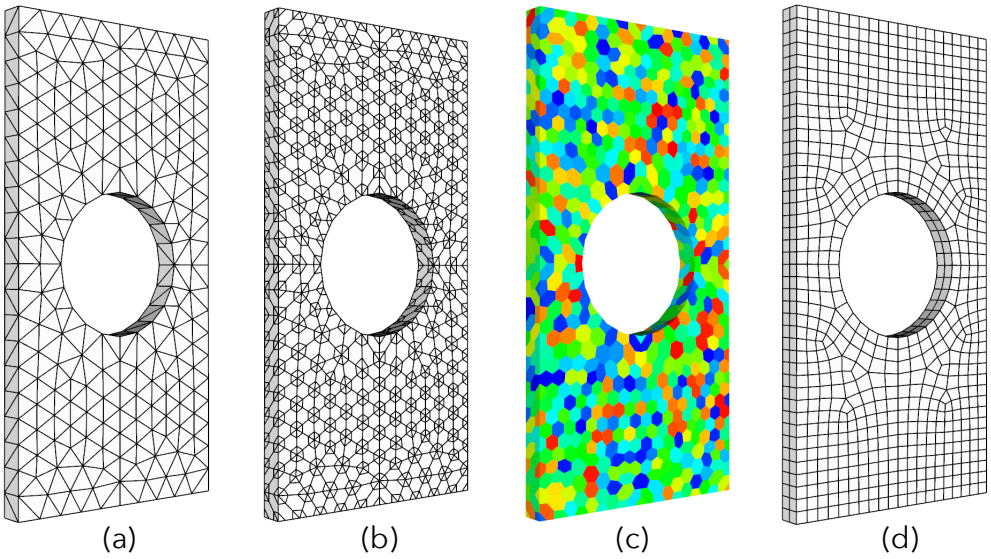

Figure 27: Polyhedral mesh of the problem of a plate with hole. (a) Initial coarse tetrahedral mesh (504 nodes, 1,492 tetrahedra), (b) type-3 polyhedral-dual mesh (5,312 nodes, 504 polytet, 1,492 octahedra), (c) random coloring of elements, and (d) a conventional hexahedral mesh (2,220 nodes, 1,320 hexahedra). Meshes refined by a factor of 4 in each dimension were used in the boundary-value problem.

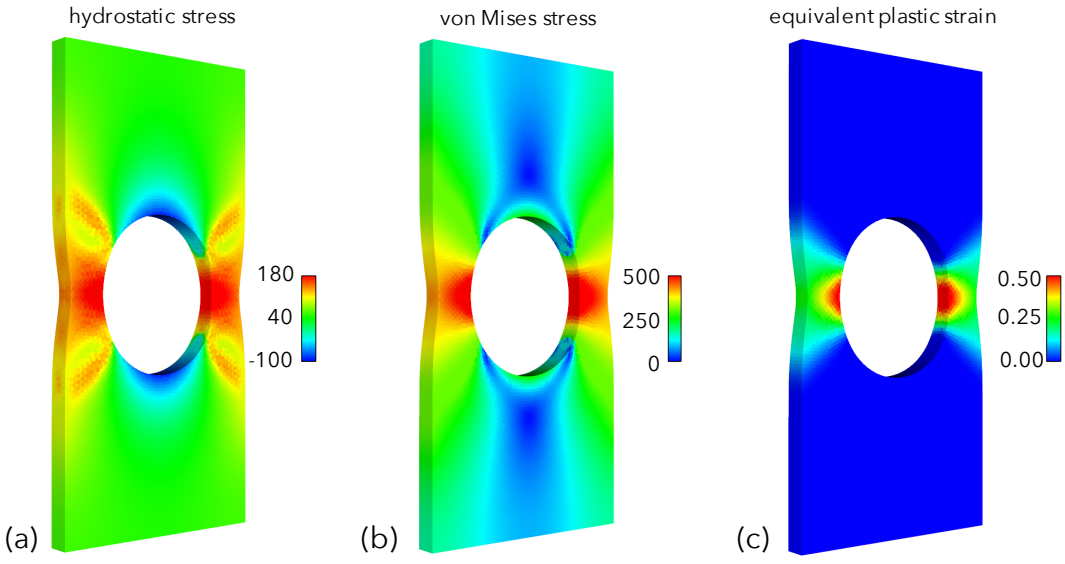

Figure 28: Simulation results for an elastic-plastic plate with hole subjected to uniaxial extension using polyhedral finite elements. (a) Pressure (MPa), (b) von Mises stress (MPa), and (c) equivalent plastic strain (263,670 nodes, 19,538 polytet, 95,116 octahedra).

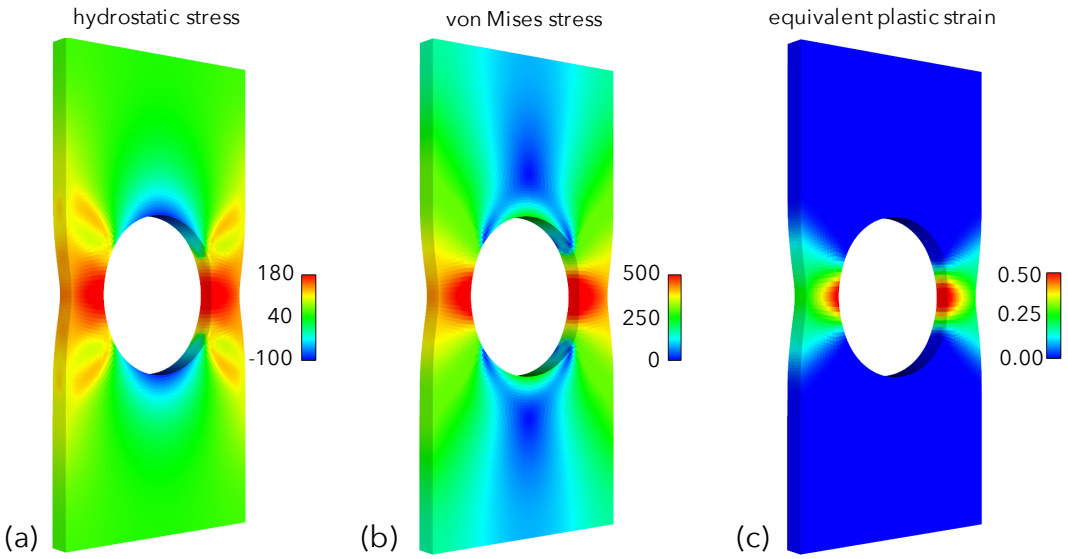

Figure 29: Simulation results for an elastic-plastic plate with hole subjected to uniaxial extension using a standard trilinear hexahedral finite elements. (a) Pressure (MPa), (b) von Mises stress (MPa), and (c) equivalent plastic strain (97, 920 nodes, 84, 480 hexahedra).

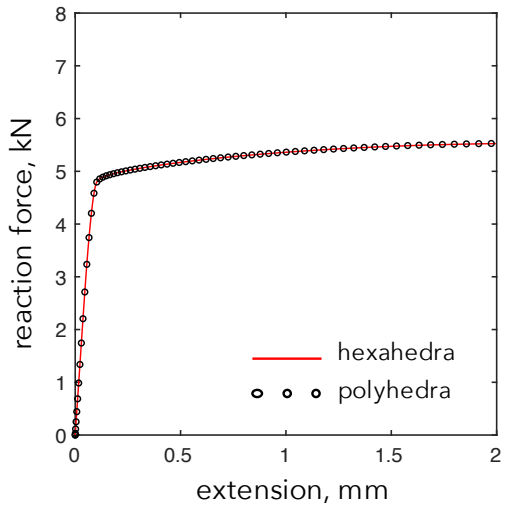

Figure 30: Comparisons of force versus deflection response of an elastic-plastic plate with hole subjected to uniaxial extension using both polyhedral and hexahedral discretizations.

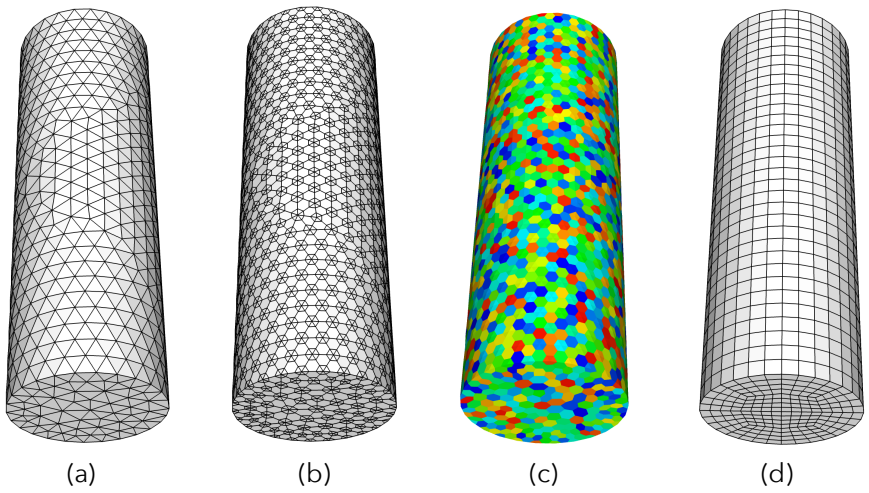

Figure 31: Polyhedral mesh of the Taylor-bar impact problem. (a) Initial tetrahedral mesh (2,395 nodes, 11,762 tetrahedra), (b) type-3 polyhedral-dual mesh (32,327 nodes, 2,395 polytet, 11,762 octahedra), (c) random coloring of elements, and (d) a conventional hexahedral mesh (6,897 nodes, 6,144 hexahedra).

The deformed cylinder 0.1 ms after impact is shown in Fig. 32 for both the polyhedral-dual mesh (left) and refined hexahedral mesh (right). The pressure field is shown on the top of the figure while the equivalent plastic strain is shown on the bottom. The pressure field is smooth for the hexahedral mesh with some evidence of oscillatory behavior for the polyhedral mesh. The hexahedral mesh results in smoother fields compared to the polyhedral mesh. The internal-state variable exhibits an oscillatory response around the impact edge for the polyhedral-dual mesh (Fig. 32c). This is possibly due to the F-bar formulation and the difference in the number of degrees of freedom between the 12-vertex polyhedra and the polyhedra formed via tetrahedral aggregation. Additional study is needed to understand this behavior.

6.4. Machine part

For the final example, we consider the linear elastic static response of the geometrically complex machine part shown in Fig. 1a. The type-3 polyhedral-dual mesh was shown in Fig. 9. Each hole is rigidly fixed while a torque is applied on the bearing surface. The resulting von Mises stress field is shown in Fig. 33b. Here, the element stresses have been averaged at the nodes to present a continuous stress field. This simulation was also performed using the max-ent shape functions for the polytet aggregates, with only small differences observed (less than 1 %).

7. Conclusions

The use of general polyhedra in engineering analysis is hampered by the lack of general-purpose polyhedral meshing algorithms and software. Here, polyhedral meshes were obtained through the use of tetrahedral subdivisions and dual cells. Each polyhedral-dual cell was formulated as a finite element with shape functions obtained through the use of both harmonic and maximum-entropy shape functions. The resulting polyhedral discretizations were used for applications in nonlinear solid mechanics using a displacement-based finite element formulation. A standard F-bar formulation was used for nearly incompressible material response. Verification examples were presented showing optimal convergence rates. Several nonlinear examples were also presented and included large deformation and plasticity. Results were comparable to those obtained using conventional hexahedral meshes. A key research question, not investigated here, is how does the efficiency and robustness of this polyhedral discretization compare to using the tetrahedral mesh directly.

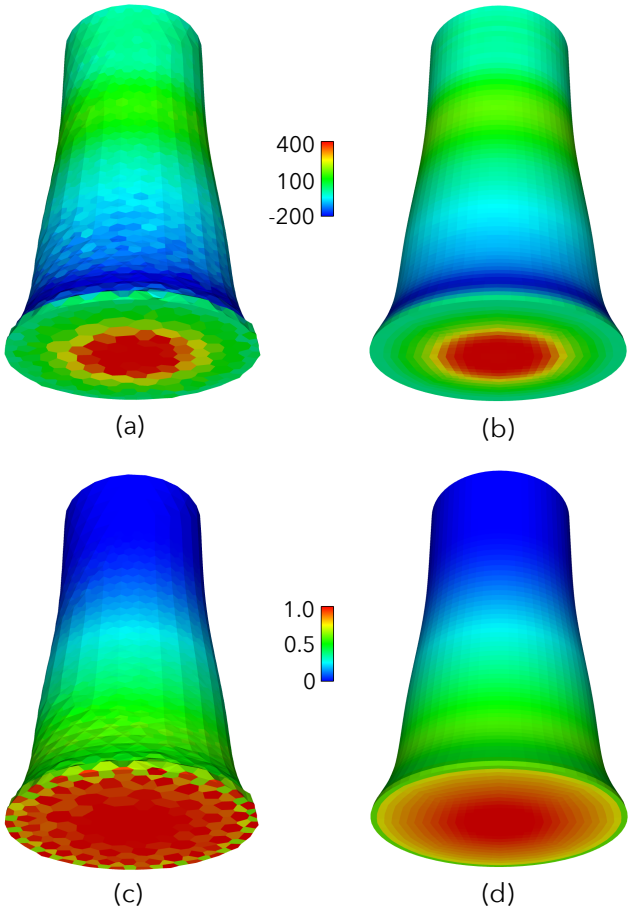

Figure 32: Simulation results for the Taylor-bar impact problem with a striking velocity of 300 m/s. (a) Pressure (MPa), polyhedral mesh, (c) equivalent plastic strain, polyhedral mesh, and (b), (d) results using a conventional hexahedral mesh (52, 065 nodes, 49, 152 hexahedra).

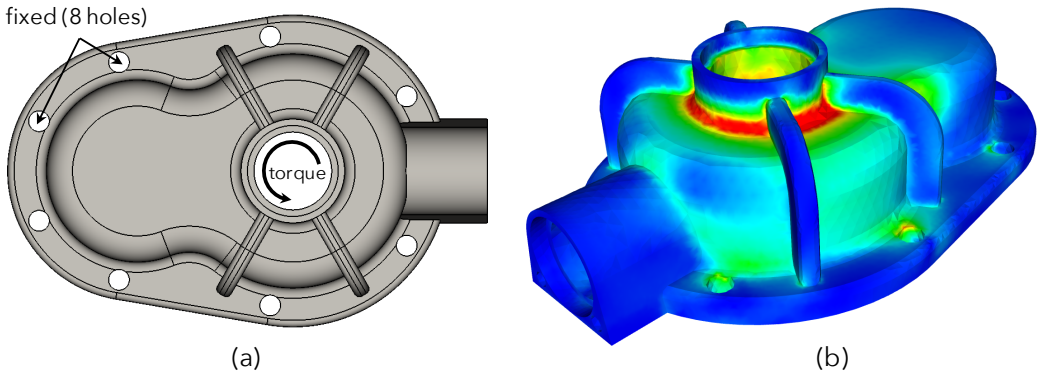

Figure 33: Stress resulting from an applied torque to the machine part shown in Fig. 1 and using the type-3 polyhedral-dual mesh shown in Fig. 9. (a) Loading and boundary conditions, and (c) smoothed von Mises stress field.

Acknowledgements

Sandia National Laboratories is a multimission laboratory managed and operated by National Technology and Engineering Solutions of Sandia, LLC, a wholly owned subsidiary of Honeywell International, Inc., for the U.S. Department of Energy's National Nuclear Security Administration under contract DE-NA-0003525. This paper describes objective technical results and analysis. Any subjective views or opinions that might be expressed in the paper do not necessarily represent the views of the U.S. Department of Energy or the United States Government.

Appendix A. Proof of derivative consistency for corrected derivatives

The process of modifying the shape function derivatives described in Section 4.2 does not corrupt the consistency properties of the derivatives given in (9). A proof of this result was given in Bishop (2014) for the case when the quadrature weights in (14) are not included. The proof still holds when the quadrature weights are included, which is established via the following theorem.

Theorem 1. *Let Ω_{e} represent an arbitrary element with volume V, boundary Γ_{e}, and vertex coordinates $\boldsymbol{X}_a$, $a = 1, \ldots, N_{\mathrm{v}}$. Consider a set of nodal shape functions $\psi_a(\boldsymbol{X})$ with linear precision so that*

$$\sum_{a=1}^{N_{\mathrm{v}}} \psi_a(\boldsymbol{X}) = 1 \,, \quad \boldsymbol{X} \in \Omega_{\mathrm{e}} \,, \tag{A.1}$$

$$\sum_{a=1}^{N_{\mathrm{v}}} \psi_a(\boldsymbol{X})\, \boldsymbol{X}_a = \boldsymbol{X} \,, \quad \boldsymbol{X} \in \Omega_{\mathrm{e}} \,. \tag{A.2}$$

Let $\{(\boldsymbol{X}_k, w_k)\,, k = 1, \ldots, N_{\mathrm{Q}}\}$ be a set of quadrature points and positive weights within Ω_{e} with the property

$$\sum_{k=1}^{N_{\mathrm{Q}}} w_k = V \,. \tag{A.3}$$

Let $\{(\boldsymbol{X}_l, w_l^{\Gamma}, \boldsymbol{N}_l)\,, l = 1, \ldots, N_{\mathrm{Q}}^{\Gamma}\}$ be a set of discrete quadrature points, positive weights, and outward unit normals on Γ_{e}, with properties (discrete divergence theorem)

$$\sum_{l=1}^{N_{\mathrm{Q}}^{\Gamma}} w_l^{\Gamma}\, \boldsymbol{N}_l = 0 \,, \tag{A.4}$$

$$\sum_{l=1}^{N_{\mathrm{Q}}^{\Gamma}} w_l^{\Gamma}\, \boldsymbol{X}_l \otimes \boldsymbol{N}_l = V \boldsymbol{I} \,. \tag{A.5}$$

The solutions $\boldsymbol{d}_{ak} \in \boldsymbol{R}^3$ of the set of constrained minimization problems

$$\min_{\boldsymbol{\xi}_k \in \boldsymbol{R}^3} \sum_{k=1}^{N_{\mathrm{Q}}} w_k ||\boldsymbol{\xi}_k - \nabla \psi_a(\boldsymbol{X}_k)||^2 \quad with \quad \sum_{k=1}^{N_{\mathrm{Q}}} w_k\, \boldsymbol{\xi}_k - \sum_{l=1}^{N_{\mathrm{Q}}^{\Gamma}} w_l^{\Gamma}\, \psi_a(\boldsymbol{X}_l)\, \boldsymbol{N}_l = 0 \tag{A.6}$$

satisfy the consistency conditions

$$\sum_{a=1}^{N_{\mathrm{v}}} \boldsymbol{d}_{ak} = 0 \,, \tag{A.7}$$

$$\sum_{a=1}^{N_{\mathrm{v}}} \boldsymbol{d}_{ak} \otimes \boldsymbol{X}_a = \boldsymbol{I} \,. \tag{A.8}$$

Proof. Let $\psi_{ak} := \psi_a(\boldsymbol{X}_k)$. The constrained minimization problem defined by (A.6) gives the modified derivatives of an individual shape function of an individual element at its volume quadrature points. This constrained minimization problem is solved for the gradient of each shape function $\nabla\psi_a$ and for each coordinate direction, independently, using the method of Lagrange multipliers (Luenberger, 2003, Ch. 10). The Lagrangian L associated with each constrained minimization problem is given by

$$L(\boldsymbol{\xi}_k, \boldsymbol{\lambda}_a) := \sum_{k=1}^{N_\mathrm{Q}} w_k ||\boldsymbol{\xi}_k - \nabla\psi_{ak}||^2 + \boldsymbol{\lambda}_a \cdot \left(\sum_{k=1}^{N_\mathrm{Q}} w_k \, \boldsymbol{\xi}_k - \sum_{l=1}^{N_\mathrm{Q}^\Gamma} w_l^\Gamma \, \psi_{al} \, \boldsymbol{N}_l \right) \tag{A.9}$$

where $\boldsymbol{\lambda}_a$ is the Lagrange multiplier vector for the given shape function. The necessary conditions for a local minimum are given by

$$\frac{\partial L}{\partial \boldsymbol{\xi}_k} = 0 \, . \tag{A.10}$$

Substituting (A.9) into (A.10) results in

$$2w_k \left(\boldsymbol{d}_{ak} - \nabla\psi_{ak} \right) + \boldsymbol{\lambda}_a w_k = 0 \, . \tag{A.11}$$

Additionally, setting to zero the partial derivative of L with respect to the Lagrange multiplier recovers the integration-consistency constraint

$$\sum_{k=1}^{N_\mathrm{Q}} w_k \, \boldsymbol{d}_{ak} - \sum_{l=1}^{N_\mathrm{Q}^\Gamma} w_l^\Gamma \, \psi_{al} \, \boldsymbol{N}_l = 0 \, . \tag{A.12}$$

The proof of the identity (A.7) is given first. Summing (A.11) from $a = 1$ to $a = N_\mathrm{v}$ results in

$$2w_k \left[\sum_{a=1}^{N_\mathrm{v}} \boldsymbol{d}_{ak} - \sum_{a=1}^{N_\mathrm{v}} \nabla\psi_{ak} \right] + w_k \sum_{a=1}^{N_\mathrm{v}} \boldsymbol{\lambda}_a = 0 \, . \tag{A.13}$$

Taking the gradient of the partition of unity relation (A.1) gives $\sum_{a=1}^{N_\mathrm{v}} \nabla\psi_a = 0$ so that the second term in the brackets in (A.13) is identically zero resulting in

$$2w_k \sum_{a=1}^{N_v} \boldsymbol{d}_{ak} + w_k \sum_{a=1}^{N_\mathrm{v}} \boldsymbol{\lambda}_a = 0 \, . \tag{A.14}$$

Summing (A.14) from $k = 1$ to $k = N_\mathrm{Q}$ gives

$$2 \sum_{k=1}^{N_\mathrm{Q}} w_k \sum_{a=1}^{N_\mathrm{v}} \boldsymbol{d}_{ak} + \sum_{k=1}^{N_\mathrm{Q}} w_k \sum_{a=1}^{N_\mathrm{v}} \boldsymbol{\lambda}_a = 0 \, . \tag{A.15}$$

Summing the integration-consistency constraint (A.12) from $a = 1$ to $a = N_\mathrm{v}$ results in

$$\sum_{a=1}^{N_\mathrm{v}} \sum_{k=1}^{N_\mathrm{Q}} w_k \, \boldsymbol{d}_{ak} - \sum_{a=1}^{N_\mathrm{v}} \sum_{l=1}^{N_\mathrm{Q}^\Gamma} w_l^\Gamma \, \psi_{al} \, \boldsymbol{N}_l = 0 \, .$$

Rearranging the summations gives

$$\sum_{k=1}^{N_\mathrm{Q}} w_k \sum_{a=1}^{N_\mathrm{v}} \boldsymbol{d}_{ak} - \sum_{l=1}^{N_\mathrm{Q}^\Gamma} w_l^\Gamma \boldsymbol{N}_l \sum_{a=1}^{N_\mathrm{v}} \psi_{al} = 0 \, . \tag{A.16}$$

From the partition of unity relation (A.1), the second summation in the second term in (A.16) is identically unity resulting in

$$\sum_{k=1}^{N_{\mathrm{Q}}} w_k \sum_{a=1}^{N_{\mathrm{v}}} \boldsymbol{d}_{ak} - \sum_{l=1}^{N_{\mathrm{Q}}^{\Gamma}} w_l^{\Gamma} \boldsymbol{N}_l = 0 \,. \tag{A.17}$$

By assumption, the discrete version of Gauss's theorem (A.4) holds so that the second term in (A.17) is identically zero. Substituting the remaining identity, $\sum_{k=1}^{N_{\mathrm{Q}}} w_k \sum_{a=1}^{N_{\mathrm{v}}} \boldsymbol{d}_{ak} = 0$, for the first term in (A.15) results in

$$\sum_{k=1}^{N_{\mathrm{Q}}} w_k \sum_{a=1}^{N_{\mathrm{v}}} \boldsymbol{\lambda}_a = 0 \,.$$

The fact that $\sum_{k=1}^{N_{\mathrm{Q}}} w_k = V > 0$ results in the identity $\sum_{a=1}^{N_{\mathrm{v}}} \boldsymbol{\lambda}_a = 0$. Substituting this identity into (A.14) and using the fact that $w_k > 0$ results in $\sum_{a=1}^{N_{\mathrm{v}}} \boldsymbol{d}_{ak} = 0$, which is the desired result, (A.7).

The proof of identity (A.8) remains. Taking the outer product of (A.11) with $\boldsymbol{X}_a$ and summing from $a = 1$ to $a = N_{\mathrm{v}}$ gives

$$2w_k \left[\sum_{a=1}^{N_{\mathrm{v}}} \boldsymbol{d}_{ak} \otimes \boldsymbol{X}_a - \sum_{a=1}^{N_{\mathrm{v}}} \nabla\psi_{ak} \otimes \boldsymbol{X}_a \right] + w_k \sum_{a=1}^{N_{\mathrm{v}}} \boldsymbol{\lambda}_a \otimes \boldsymbol{X}_a = 0 \,. \tag{A.18}$$

Taking the gradient of (A.2) results in $\sum_{a=1}^{N_{\mathrm{v}}} \nabla\psi_a \otimes \boldsymbol{X}_a = \boldsymbol{I}$. Substituting this result for the second term in the brackets in (A.18) gives

$$2w_k \left[\sum_{a=1}^{N_{\mathrm{v}}} \boldsymbol{d}_{ak} \otimes \boldsymbol{X}_a - \boldsymbol{I} \right] + w_k \sum_{a=1}^{N_{\mathrm{v}}} \boldsymbol{\lambda}_a \otimes \boldsymbol{X}_a = 0 \,. \tag{A.19}$$

Summing (A.19) from $k = 1$ to $k = N_{\mathrm{Q}}$ results in

$$2 \left[\sum_{k=1}^{N_{\mathrm{Q}}} w_k \sum_{a=1}^{N_{\mathrm{v}}} \boldsymbol{d}_{ak} \otimes \boldsymbol{X}_a - \boldsymbol{I} \sum_{k=1}^{N_{\mathrm{Q}}} w_k \right] + \sum_{k=1}^{N_{\mathrm{Q}}} w_k \sum_{a=1}^{N_{\mathrm{v}}} \boldsymbol{\lambda}_a \otimes \boldsymbol{X}_a = 0 \,. \tag{A.20}$$

From (A.3), the sum in the second term in the brackets in (A.20) is identically V so that

$$2 \left[\sum_{k=1}^{N_{\mathrm{Q}}} w_k \sum_{a=1}^{N_{\mathrm{v}}} \boldsymbol{d}_{ak} \otimes \boldsymbol{X}_a - V\boldsymbol{I} \right] + \sum_{k=1}^{N_{\mathrm{Q}}} w_k \sum_{a=1}^{N_{\mathrm{v}}} \boldsymbol{\lambda}_a \otimes \boldsymbol{X}_a = 0 \,. \tag{A.21}$$

Taking the outer product of the integration-consistency constraint (A.12) with $\boldsymbol{X}_a$ and summing from $a = 1$ to $a = N_{\mathrm{v}}$ gives

$$\sum_{a=1}^{N_{\mathrm{v}}} \sum_{k=1}^{N_{\mathrm{Q}}} w_k \, \boldsymbol{d}_{ak} \otimes \boldsymbol{X}_a - \sum_{a=1}^{N_{\mathrm{v}}} \sum_{l=1}^{N_{\mathrm{Q}}^{\Gamma}} w_l^{\Gamma} \, \psi_{al} \, \boldsymbol{N}_l \otimes \boldsymbol{X}_a = 0 \,.$$

Rearranging the summations gives

$$\sum_{k=1}^{N_{\mathrm{Q}}} w_k \sum_{a=1}^{N_{\mathrm{v}}} \boldsymbol{d}_{ak} \otimes \boldsymbol{X}_a - \sum_{l=1}^{N_{\mathrm{Q}}^{\Gamma}} w_l^{\Gamma} \boldsymbol{N}_l \otimes \sum_{a=1}^{N_{\mathrm{v}}} \psi_{al} \boldsymbol{X}_a = 0 \,. \tag{A.22}$$

From (A.2), the second summation in the second term in (A.22) is identically $\boldsymbol{X}_l$ resulting in

$$\sum_{k=1}^{N_{\mathrm{Q}}} w_k \sum_{a=1}^{N_{\mathrm{v}}} \boldsymbol{d}_{ak} \otimes \boldsymbol{X}_a - \sum_{l=1}^{N_{\mathrm{Q}}^{\Gamma}} w_l^{\Gamma} \boldsymbol{N}_l \otimes \boldsymbol{X}_l = 0 \,. \tag{A.23}$$

By assumption, the discrete version of Gauss's theorem is valid, (A.5), so that the second term in (A.23) is identically $V\boldsymbol{I}$. Equation (A.23) then reduces to

$$\sum_{k=1}^{N_{\mathrm{Q}}} w_k \sum_{a=1}^{N_{\mathrm{v}}} \boldsymbol{d}_{ak} \otimes \boldsymbol{X}_a = V\boldsymbol{I} \ .$$

Substituting this expression for the first term in the brackets in (A.21), results in the bracketed term vanishing. The remaining term gives the identity

$$\sum_{k=1}^{N_{\mathrm{Q}}} w_k \sum_{a=1}^{N_{\mathrm{v}}} \boldsymbol{\lambda}_a \otimes \boldsymbol{X}_a = 0 \ .$$

Again, the fact that $\sum_{k=1}^{N_{\mathrm{Q}}} w_k = V > 0$ results in $\sum_{a=1}^{N_{\mathrm{v}}} \boldsymbol{\lambda}_a \otimes \boldsymbol{X}_a = 0$. Substituting this identity into (A.19) and using the fact that $w_k > 0$ gives $\sum_{a=1}^{N_{\mathrm{v}}} \boldsymbol{d}_{ak} \otimes \boldsymbol{X}_a = \boldsymbol{I}$, which is the desired result given by (A.8). □

References

Abdelkader, A., Bajaj, C.L., Ebeida, M.S., Mahmoud, A.H., Mitchell, S.A., Owens, J.D., Rushdi, A.A., 2019. VoroCrust: Voronoi meshing without clipping. arXiv preprint arXiv:1902.08767 .

Arroyo, M., Ortiz, M., 2006. Local maximum-entropy approximation schemes: a seamless bridge between finite elements and meshfree methods. International Journal for Numerical Methods in Engineering 65, 2167–2202.

Balafas, G., 2014. Polyhedral mesh generation for CFD-analysis of complex structures. Master's thesis. Technische Universität München.

Barber, J.R., 2010. Elasticity. Springer, New York, NY.

Bassi, F., Botti, L., Colombo, A., Pietro, D.A.D., Tesini, P., 2012. On the flexibility of agglomeration based physical space discontinuous Galerkin discretizations. Journal of Computational Physics 231, 45–65.

Bathe, K.J., 1996. Finite Element Procedures. Prentice Hall, Englewood Cliffs, NJ.

Beirão da Veiga, L., Brezzi, F., Cangiani, A., Manzini, G., Marini, L.D., Russo, A., 2013. Basic principles of Virtual Element Methods. Mathematical Models and Methods in Applied Sciences 23, 199–214.

Belytschko, T., Liu, W.K., Moran, B., Elkhodary, K., 2014. Nonlinear Finite Elements for Continua and Structures. second ed., Wiley, London, UK.

Bishop, J.E., 2009. Simulating the pervasive fracture of materials and structures using randomly close packed Voronoi tessellations. Computational Mechanics 44, 455–471.

Bishop, J.E., 2014. A displacement-based finite element formulation for general polyhedra using harmonic shape functions. International Journal for Numerical Methods in Engineering 97, 1–31.

Bishop, J.E., 2019. A kinematic comparison of mesh-free and mesh-based lagrangian approximations using manufactured extreme-deformation fields. Computational Particle Mechanics (submitted).

Bishop, J.E., Martinez, M.J., Newell, P., 2016. Simulating fragmentation and fluid-induced fracture in disordered media using random finite-element meshes. International Journal for Multiscale Computational Engineering 14, 349–366.

Bonet, J., Wood, R., 2008. Nonlinear Continuum Mechanics for Finite Element Analysis. second ed., Cambridge University Press, Cambridge, UK.

Cangiani, A., Manzini, G., Russo, A., Sukumar, N., 2015. Hourglass stabilization and the virtual element method. International Journal for Numerical Methods in Engineering 102, 404–436.

Chen, J.S., Wu, C.T., Yoon, S., You, Y., 2001. A stabilized conforming nodal integration for Galerkin mesh-free methods. International Journal for Numerical Methods in Engineering 50, 435–466.

Chi, H., Beirão da Veiga, L., Paulino, G.H., 2017. Some basic formulations of the virtual element method (VEM) for finite deformations. Computer Methods in Applied Mechanics and Engineering 318, 148–192.

Chin, E.B., Bishop, J.E., Garimella, R.V., Sukumar, N., 2018. Finite deformation cohesive polygonal finite elements for modeling pervasive fracture. International Journal of Fracture 214, 139–165.

Cubit, 2018. CUBIT Geometry and Meshing Toolkit, Version 15.1. `https://cubit.sandia.gov`.

Danielson, K., 2014. Fifteen node tetrahedral elements for explicit methods in nonlinear solid dynamics. Computer Methods in Applied Mechanics and Engineering 272, 160–180.

Eterovic, A.L., Bathe, K.J., 1990. A hyperelastic-based large strain elasto-plastic constitutive formulation with combined isotropic-kinematic hardening using the logarithmic stress and strain measures. International Journal for Numerical Methods in Engineering 30, 1099–1114.

Flanagan, D.P., Belytschko, T., 2015. A uniform strain hexahedron and quadrilateral with orthogonal hourglass control. International Journal for Numerical Methods in Engineering 17, 679–706.

Gain, A.L., Talischi, C., Paulino, G.H., 2014. On the Virtual Element Method for three-dimensional linear elasticity problems on arbitrary polyhedral meshes. Computer Methods in Applied Mechanics and Engineering 282, 132–160.

Gao, X., Jakob, W., Tarini, M., Panozzo, D., 2017. Robust hex-dominant mesh generation using field-guided polyhedral agglomeration. ACM Transactions on Graphics 36, 1–13.
Garimella, V.R., Kim, J., Berndt, M., 2014. Polyhedral mesh generation and optimization for non-manifold domains, in: Sarrate, J., Staten, M. (Eds.), Proceedings of the 22nd International Meshing Roundtable, Springer International Publishing. pp. 313–330.
Hinton, E., Rock, T., Zienkiewicz, O.C., 1976. A note on mass lumping and related processes in the finite element method. Earthquake Engineering and Structural Dynamics 4, 245?249.
Hormann, K., Sukumar, N., 2008. Maximum entropy coordinates for arbitrary polytopes. Computer Graphics Forum 27, 1513–1520.
Hormann, K., Sukumar, N. (Eds.), 2018. Generalized Barycentric Coordinates in Computer Graphics and Computational Mechanics. CRC Press, New York, NY.
Hughes, T.J.R., 2000. The Finite Element Method: Linear Static and Dynamic Finite Element Analysis. Dover, New York, NY.
Joshi, P., Meyer, M., DeRose, T., Green, B., Sanocki, T., 2007. Harmonic coordinates for character articulation. ACM Transactions on Graphics 26. Article 71.
Kim, H.G., Sohn, D., 2015. A new finite element approach for solving three-dimensional problems using trimmed hexahedral elements. International Journal for Numerical Methods in Engineering 102, 1527–1553.
Koester, J.J., Chen, J.S., 2019. Conforming window functions for meshfree methods. Computer Methods in Applied Mechanics and Engineering 347, 588–621.
Korelc, J., Wriggers, P., 1996. Consistent gradient formulation for a stable enhanced strain method for large deformations. Engineering Computations 13, 103–123.
Krongauz, Y., Belytschko, T., 1997. Consistent pseudo-derivatives in meshless methods. Computer Methods in Applied Mechanics and Engineering 146, 371–386.
Lee, S.Y., 2015. Polyhedral mesh generation and a treatise on concave geometrical edges. Procedia Engineering 124, 174–186.
Liu, Y., Saputra, A.A., Wang, J., Tin-Loi, F., Song, C., 2017. Automatic polyhedral mesh generation and scaled boundary finite element analysis of STL models. Computer Methods in Applied Mechanics and Engineering 313, 106–132.
Luenberger, D., 2003. Linear and Nonlinear Programming. Second ed., Kluwer Academic Publishers, Boston, MA.
Martin, S., Kaufmann, P., Botsch, M., Wicke, M., Gross, M., 2008. Polyhedral finite elements using harmonic basis functions. Computer Graphics Forum 27, 1521–1529.
Millán, D., Sukumar, N., Arroyo, M., 2015. Cell-based maximum-entropy approximants. Computer Methods in Applied Mechanics and Engineering 284, 712–731.
Oaks, W., Paoletti, S., 2000. Polyhedral mesh generation, in: International Meshing Roundtable, pp. 57–67.
Ostien, J.T., Foulk, J.W., Mota, A., Veilleux, M.G., 2016. A 10-node composite tetrahedral finite element for solid mechanics. International Journal for Numerical Methods in Engineering 107, 1145–1170.
Rashid, M.M., Selimotic, M., 2006. A three-dimensional finite element method with arbitrary polyhedral elements. International Journal for Numerical Methods in Engineering 67, 226–252.
Rimoli, J.J., Ortiz, M., 2011. A duality-based method for generating geometric representations of polycrystals. International Journal for Numerical Methods in Engineering 86, 1069–1081.
Sohn, D., Cho, Y.S., Im, S., 2012. A novel scheme to generate meshes with hexahedral elements and poly-pyramid elements: The carving technique. Computer Methods in Applied Mechanics and Engineering 201-204, 208–227.
Sohn, D., Cho, Y.S., Im, S., 2013. A finite element scheme with the aid of a new carving technique combined with smoothed integration. Computer Methods in Applied Mechanics and Engineering 254, 42–60.
Sokolov, D., Ray, N., Untereiner, L., Lévy, B., 2016. Hexahedral-dominant meshing. ACM Transactions on Graphics 35, 1–23.
de Souza Neto, E.A., Perić , D., Owen, D.R.J., 2008. Computational Methods for Plasticity: Theory and Applications. Wiley, Chichester, UK.
Sukumar, N., 2004. Construction of polygonal interpolants: a maximum entropy approach. International Journal for Numerical Methods in Engineering 61, 2159–2181.
Sukumar, N., Malsch, E.A., 2006. Recent advances in the construction of polygonal finite element interpolants. Archives of Computational Methods in Engineering 13, 129–163.
Sukumar, N., Wright, R.W., 2007. Overview and construction of meshfree basis functions: from moving least squares to entropy approximants. International Journal for Numerical Methods in Engineering 70, 181–205.
Talebi, H., Saputra, A., Song, C., 2016. Stress analysis of 3D complex geometries using the scaled boundary polyhedral finite elements. Computational Mechanics 58, 697–715.
Talischi, C., Pereira, A., Menezes, I.F.M., Paulino, G.H., 2015. Gradient correction for polygonal and polyhedral finite elements. International Journal for Numerical Methods in Engineering 102, 728–747.
Taylor, G., 1948. The use of flat-ended projectiles for determining dynamic yield stress I. Theoretical considerations. Proceedings of the Royal Society of London 194, 289–299.
Wachspress, E., 1975. A Rational Finite Element Basis. volume 114 of *Mathematics in Science and Engineering*. Academic Press, New York, NY.
Wicke, M., Botsch, M., Gross, M., 2007. A finite element method on convex polyhedra. Computer Graphics Forum 26, 355–364.
Wriggers, P., Rust, W.T., Reddy, B.D., 2016. A virtual element method for contact. Computational Mechanics 58, 1039–1050.